CHAPTER 4

Theoretical Modelling and Analyses of Emerging Copper-based Solar Cell Materials

R. Chen,[a,b] S. Zamulko[b] and C. Persson[b,c,*]

[a] Uppsala University, Department of Engineering Sciences, P.O. Box 256, Uppsala, 75105, Sweden

[b] University of Oslo, Department of Physics / Centre for Materials Science and Nanotechnology, P.O. Box 1048 Blindern, Oslo, 0316, Norway

[c] KTH Royal Institute of Technology, Department of Materials Science and Engineering, Stockholm, 10044, Sweden

*Corresponding contributor. E-mail: Clas.Persson@fys.uio.no

Abstract

Herein we investigate the structural, electronic, and optical properties of emerging copper-based chalcogenides, employing atomistic first-principles computational method within the density functional theory. The fundamental material characteristics of the compounds are analysed, and the optoelectronic performances are improved by alloying with isovalent elements. In order to develop inorganic photovoltaics based on ultrathin photon-absorbing film (i. e., with thicknesses $d < 100$ nm), the material shall exhibit optimized band-gap energy E_g as well as having a very high absorption coefficient $\alpha(\omega)$, especially for photons energies in the lower spectrum: $E_g \leq E < (E_g + 2\ \text{eV})$. To develop high-efficient solar cells we therefore suggest to tailor-make the materials to form direct gap multi-valley band edges, and energy bands with rather flat dispersions. That can typically be achieved by considering alloys with heavy elements that have relatively localized *sp*-like orbitals. With such tailored materials, we demonstrate that it is possible to reach a theoretical maximum efficiency as high as $\eta_{max} \approx 30\%$ for film thicknesses of $d \approx 50$–100 nm.

4.1 Introduction

In this work, we theoretically investigate inorganic solar cell materials by means of first-principles atomistic methods within the framework of the density functional theory (DFT). The aim is to further accelerate the progress of developing environmentally friendly p-n junction photovoltaics (PV), especially towards technologies with high-efficient and inexpensive ultrathin films. Crystalline silicon (c-Si) is today by far the most commercialized materials in PV modules with above 90% of the market [1], despite having indirect gap with band-gap energy $E_g \approx 1.2$ eV. For laboratory solar cell, the energy conversion efficiency for single crystal c-Si without concentrator is η_{max} = 25.8% (Rev. 10-30-2017 [2]), but the active absorber material is rather thick, often 100–200 μm due to insufficient absorption. Thin-film PV technologies rely on 100 times thinner layer (typically around 1 μm), and the absorbers must therefore have higher capacity to absorb the sunlight in the energy region from ~1 to ~3 eV. The most traditional inorganic solar cells [2] are based on either amorphous silicon (a-Si or its hydrogenated compound a-Si:H with E_g = 1.7 eV and η_{max} = 14.0%), cadmium telluride (CdTe; E_g = 1.5 eV and η_{max} = 22.1%), thin-film gallium arsenide (GaAs; E_g = 1.5 eV and η_{max} = 28.8%), or copper indium gallium selenide ($CuIn_{1-x}Ga_xSe_2$; $E_g \approx 1.2$ eV for x = 0.3 and η_{max} = 22.6%), and these materials have their “pros and cons” in terms of prospective large-scale production. Developments of even thinner absorber materials, i.e., for ultrathin inorganic solar cells, is an emerging concept to produce competitive PV cells or to complement the c-Si technologies with a proper top-cell in tandem structures. Here, ultrathin implies absorber layers with thicknesses less than 100 nm (perhaps as thin as 10–30 nm), which is then at least more than 10 times thinner than in the traditional thin-film technologies. Ultrathin layers will not only be lighter and save material, fabrication, and handling costs, but they also imply shorter path for the photon-excited carriers to reach the electrodes. An ultrathin solar cell material is expected to be not only have very high ability to absorb the sunlight, but also (as for the traditional PV technologies) to be environmentally friendly and of low cost. It requires not only that the cost of syntheses, manufacturing process, recycling, and handling of the modules shall be sufficiently low, but also that the device shall have a long operating lifetime. Moreover, the raw material elements shall be Earth abundant, non-toxic, and inexpensive. In addition to that, the materials shall be thermodynamic stable even in operation, easily to doped or be natively p- or n-type, it shall contain no devastating defects, have high carrier mobility, as well as to have good interface physics with proper band alignment with the other device layers.

In that perspective, the copper-based chalcogenides can be regarded as attractive absorber materials for the developments of ultrathin devices. Chalcopyrite copper indium gallium selenide ($CuIn_{1-x}Ga_xSe_2 \equiv$ CIGS) is today a commercially important thin-film PV material ($\eta_{max} \approx$ 22.6% [2]), and it is also a very intriguing material from a scientific point of view [3-7]. Kesterite copper zinc tin sulphide/selenide ($Cu_2ZnSnS_4 \equiv$ CZTS and $Cu_2ZnSnSe_4 \equiv$ CZTSe) is considered as an alternative absorber material to CIGS with the advantage to not involve indium which is a costly element [8-13]. Its solar cell efficiency is to date some 10% lower than that of CIGS, that is η_{max} = 12.6% [2]. Attempts to improve the device efficiency to optimize the band gap

energy as well as to form a built-in electric field arising from a compositional grading of the materials (e.g., $Cu_2ZnSn(S_{1-x}Se_x)_4 \equiv$ CZTSSe and $Cu_2Zn(Sn_{1-x}Ge_x)S_4 \equiv$ CZTGS) have shown some enhanced effects on the optoelectronic performances [14-21]. One of the earliest recognized solar-cell materials (already in the 1920s, thus long before the Si technologies) is cuprous oxide Cu_2O [22], but the material quality and the PV performance were rather poor in the attempts to develop low-cost devices in the 1970s [23]. Today, the compound is again relevant, especially as a top-cell in a device structure. Based on the many good basic qualities of these copper-based chalcogenides, and the ability to fabricate rather inexpensive PV devices with polycrystalline, non-stoichiometric, as-grown p-type materials, it can motivate to further explore copper-based chalcogenides. For example, ternary Cu-group-IV chalcogenides, like the Cu_2SnS_3 (CTS) compound [24-30] or perhaps corresponding Sn/Ge-poor $Cu_4(Sn/Ge)S_4$ phase [31-34] are candidates as solar cell absorber material. From that, also their relevant isovalent cation alloys $Cu_2Sn_{1-x}Ge_xSe_3$ (CTGS) and perhaps also $Cu_2Sn_{1-x}Si_xSe_3$ (CTSS) can be attractive due to the tuneable band gap energies [35,36]. An alternative to cation alloying as in CTSS, also anion alloying can be utilize to optimize both band gap energy and energy position of the valence band maximum (VBM). Here, $Cu(Sb/Bi)S_2$ with heavy group-V elements Sb or Bi, that is, either $CuSbS_2$ (CSS) or $CuBiS_2$ (CBS) as ternary compound [37-44], can be the base compound for alloying in order to tune the electronic band edges, for example the $CuSb(Se_{1-x}Te_x)_2$ alloy (CSST) and the $CuBi(S_{1-x}Se_x)_2$ alloy (CBSS), [45]. Also Sb/Bi poor phases $Cu_3(Sb/Bi)S_3$ are interesting for wide-gap solar cell material [46-50]. With a proper choice of the cation and anion alloying configurations, both the VBM and the conduction band minimum (CBM) can be optimized for the overall band profile of the solar cell device involving also the buffer layers, window layer as well as the electrodes. One can, at the same time, to certain extend also minimize the lattice mismatching between the absorber and buffer layers. (This can also be done by choice of proper buffer layer material.)

Utilizing the DFT [51] in conjunction with the Kohn-Sham equation (KS-eq. [52]) we theoretically model and explore several of these emerging Cu-based chalcogenides (i. e., Cu-*X*-(O/S/Se/Te) and also some of their isovalent alloys) based on first-principles atomistic calculations using the projector augmented wave (PAW) and the full-potential, augmented plane wave (APW) formalisms as implemented in VASP [53,54] and WIEN2k [55] program packages, respectively. The calculations rely on the exchange-correlation potentials that are described by the generalized gradient approximations by Perdew, Burke, and Ernzerhof (PBE) [56] and the corresponding functional revised for solids (PBEsol) [57], both with or without an onsite Coulomb interaction correction U_d [58] of the *d*-like orbitals for the transition metal atoms (i.e., the PBE+U and PBEsol+U approaches), as well as the hybrid functional by Heyd, Scuseria, and Ernzerhof (HSE06) [59,60].

The crystalline structures of the compounds are determined from total energy calculations; examples of the different crystalline structures are depicted in Figure 4.1. The electronic properties are analysed in terms of the electronic structures of the topmost valence bands (VBs) and the bottommost conduction bands (CBs), the fundamental band gap energy, as well as of the total density-of-states (DOS) with a detailed description from

the atom and angular-momentum resolved DOS (i. e., PDOS). The optical properties are analysed in terms of the complex dielectric function $\varepsilon(E) = \varepsilon_1(E) + i\varepsilon_2(E)$ and the absorption coefficient $\alpha(E)$. The very high absorption coefficients in the energy region $E_g \leq E < (E_g + 2\ \text{eV})$ for certain Cu-based chalcogenides are directly explained by the electronic band structures, and these compounds are highly relevant for further investigation and developments of ultrathin solar cells. Moreover, detailed analysis of especially the CTS compound reveals that a very dense **k**-mesh of the irreducible Brillouin zone (IBZ) is needed in the calculations in order to fully describe the optical properties of this material.

[Figure 4.1 near here]

The performance of the materials as a solar cell absorber is analysed within the Shockley-Queisser (SQ) model for the theoretical limit of the maximum efficiency η_{max}, considering a single p-n junction structure described by the Shockley ideal diode equation. We include a thickness dependence of the absorptivity in the model, and we then describe how the maximum efficiency decreases when the absorber layer is thinner. From that analyses, we can tailor-make emerging solar cell materials that have sufficiently high efficiency also for ultrathin thicknesses, and we suggest that one shall design materials with direct gap multi-valley band edges, and energetically topmost VBs as well as the bottommost CBs shall have rather flat energy dispersions. That can be achieved by, for instance, considering compounds with heavy elements, since those elements have typically energetically more localized orbitals. We compare the results for the emerging Cu-based chalcogenides with corresponding data of the traditional thin-film solar cell materials, demonstrating the possibilities to develop high-efficient ultrathin solar cell devices. That is, it is possible to design absorber materials with the theoretical maximum efficiency as high as $\eta_{max} \approx 30\%$ for film thicknesses of $d \approx 50$–100 nm. However, it is important that the flat band dispersions in these materials do not form indirect gap with energy smaller than that of the fundamental direct gap, because the Auger effect can then lower the efficiency by some 3% to 5%.

4.2 Computational Methods

The computational method are based on the ground-state DFT [51] as realized with the KS-eq [52]. The DFT is based on two main theorems, i. e., the Hohenberg-Kohn theorems. The first theorem states that the density of the system determines all ground-state properties of that system. The second theorem states that there exists a variational principle for the energy density functional, such that the ground-state total energy can be obtained by varying the density. Thus, there exists a universal function for the total energy $E_{tot}[n]$ of the electron density $n(\mathbf{r})$ for all electron systems, and it is obtained through $E_{tot}[n_0] < E_{tot}[n]$ where n_0 is the ground-state density. The idea of the DFT is to consider only the electron density in the material instead of using the complex many-electron wave function, and this would be a huge simplification of the problem. However, the Hohenberg-

Kohn theorems do not tell us the form of $E_{tot}[n]$, and the expression of the functional is to date unknown.

The KS-eq is derived from the DFT, and it is a method to solve the DFT in principle exactly. The approach relies however on auxiliary Kohn-Sham (KS) single-electron eigefunctions $\psi_i^{KS}(\mathbf{r})$ to generate the exact total density $n(\mathbf{r})$ of the system. Assuming the corresponding auxiliary many-electron wave function is Hartree-like, then the KS-eq reads

$$\left\{-\frac{\hbar^2}{2m_e}\nabla^2 + V_{eff}(\mathbf{r})\right\}\psi_i^{KS}(\mathbf{r}) = \varepsilon_i^{KS}\psi_i^{KS}(\mathbf{r}) \tag{4.1}$$

$$V_{eff}(\mathbf{r}) = V_H(\mathbf{r}) + V_{en}(\mathbf{r}) + V_{xc}(\mathbf{r}) \tag{4.2}$$

$$E_{tot}[n] = \sum_i \varepsilon_i^{KS} - \frac{1}{2}\int\int q^2 \frac{n(\mathbf{r})n(\mathbf{r}')}{|\mathbf{r}-\mathbf{r}'|}d\mathbf{r}d\mathbf{r}' + E_{xc}[n] - \int V_{xc}(\mathbf{r})n(\mathbf{r})d\mathbf{r} \tag{4.3}$$

$$n(\mathbf{r}) = \sum_i \left|\psi_i^{KS}(\mathbf{r})\right|^2 \qquad i = 1, 2, \ldots, N_e \text{ for the } N_e \text{ occupied electronic states.} \tag{4.4}$$

Here, the effective potential $V_{eff}(\mathbf{r})$ comprises the well-defined Hartree potential $V_H(\mathbf{r})$, the system dependent external electron-nuclei interaction potential $V_{en}(\mathbf{r})$, and the so-called exchange-correlation potential $V_{xc}(\mathbf{r})$. The KS-eq is an approach to map the many-electron problem into many single-electron equations with an effective potential $V_{eff}(\mathbf{r})$. The effective potential includes all electron-electron interactions (but also some part of the electrons' kinetic energies). The advantage of describing all the electron-electron interactions by an effective potential is immense. Importantly, the derivation proves that it is possible to generate the exact ground-state density and the exact ground-state total energy if one finds the universal expression of the effective potential that correctly includes the many-electron interactions. It is worth remarking here that the KS-eq is typically Fourier transformed and solved in the reciprocal space (**k**-space) in order to benefit from translation symmetry of period system, as considered in this work. The eigenfunctions and the corresponding eigenvalues are then represented for the j:th energy band at the specific quantum state **k**, thus $\psi_{j,\mathbf{k}}^{KS}(\mathbf{r})$ and $\varepsilon_{j,\mathbf{k}}^{KS}(\mathbf{r})$, and the superscript KS is often neglected.

The KS-eq in the DFT is in principle an exact method. However, we have to date not the full explicit expression of the universal exchange-correlation potential $V_{xc}(\mathbf{r})$ that shall include the often complex many-electron interactions. Here lies the main approximation within the Kohn-Sham approach: one has to rely on approximations of the exchange-correlation potential, and the local density approximation (LDA) is the first model of $V_{xc}(\mathbf{r})$. The approximation is based on the free electron gas, and it uses locally the exact description

of the exchange-correlation of a homogeneous electron gas (free electron gas or "jellium"). Despite its simplicity, LDA has however been extremely successful to describe the many-electron interactions, although the approximation has deficiencies. Also, many improved approximations beyond the LDA are available, for example the generalized gradient approximation (GGA) wherein also the gradient of the electron density is taken into account. The LDA and GGA are fairly accurate methods, but have limitations in terms of inaccurate band gap energies and localization of *d*- and *f*-like states. Development of further improved exchange-correlation potential is still an ongoing and important research activity. Hybrid functional is an approach that mixes two or more types of exchange-correlation functionals, very often with a contribution from pure non-local Fock exchange potential to localize states, in order to optimize the computed material properties, especially the band gap energies as obtained from the single-electron energies. The LDA+U (or GGA+U) are methods to include a Hubbard-like on-site Coulomb correction potential to the DFT exchange-correlation potential in order to better describe strongly localized (strongly correlated) *d*-and *f*-systems.

Since the exchange-correlation potential $V_{xc}(\mathbf{r})$ is not exact, the total energy and the KS single-electron energies and eigenfunctions are not exact. However, the existing approximations to $V_{xc}(\mathbf{r})$ normally yield very good results. The drawback is the band gap energies E_g for semiconductors and insulators, which are underestimated by typically 50%. Approaches to more accurate determine the E_g (like, for example, the hybrid functionals with non-local Fock exchange) are often very time and computational demanding, especially for systems with many atoms in the unit cells. Furthermore, even with an exact description of the exchange-correlation potential, the auxiliary KS single-electron and the corresponding total wave functions are not described exactly, since the KS-eq uses (in the approach above) a Hartree-like form of the total wave function, and thus its single-electron energies cannot be exact. Hence, if one determines the band gap energy from the KS eigenfunctions (instead of from total energies), one shall not expect to obtain the exact gap energy even for the exact $V_{xc}(\mathbf{r})$. However, it is believed that the KS eigenfunctions fairly accurately can describe the true single-electron wave functions.

DFT in conjunction with the KS-eq, and with different types of approximations for the exchange-correlation potential, has during the last 40 years been extremely successful to describe systems with a large number of atoms, like for instance solids, nanostructures, and large molecules. Employing the DFT, theoreticians in material physics and chemistry are supporting experimental studies, analysing the underlying physics of many-atom systems, as well as exploring new material and molecular structures. The DFT is one of the most popular approaches to explore many-atoms systems, and in 1998, Prof. John A. Pople and Prof. Walter Kohn shared the Nobel Prize in Chemistry for their contributions to develop the DFT and computational methods.

4.2.1 Basic Computational Details

The calculations of crystalline, electronic and optical properties are based on KS approach to solve the ground-state DFT. The approaches rely on either the PAW basis set in the VASP package [53,54] or the FPLAPW basis set in the WIEN2k package [55]. Unless specifically stated, the following described computational method and computational parameters are used.

The compounds and their crystalline structures are presented in Figure 4.1. The compounds are modelled with their primitive cells by the PAW potentials as a generalization of the pseudopotential formalisms. The crystalline structures are fully relaxed until the total energy and the residual force on each atom from the quasi-Newton algorithm show convergence within 0.1 meV and 10 meV/Å, respectively, using the hybrid functional HSE06 with the standard parameters for mixing and screening [59,60], i. e., 25% non-local Fock exchange for the short-range interactions with the range separation of 0.2 $Å^{-1}$.

The total energy as well as the total DOS and the local, atomic- and angular-resolved DOS (i. e.., PDOS) were obtained from the modified tetrahedron integration method with a Γ-centered Monkhorst-Pack like **k**-mesh. For cubic crystal structures with 8 atoms per primitive cell, we use typically **k**-mesh grids of the size of 6×6×6 in the IBZ, and the grid sizes change inversely with the cell sizes. We excluded the spin orbit coupling (SOC), unless when SOC causes strong effect on the band dispersions, because typically there are no SOC induced energy split in the degeneracies at the band edges that can cause strong impact on the dispersion. SOC can for some materials with heavy elements narrow the band-gap energy, but by only 0.1–0.2 eV, and such effect does not change the materials from being indirect to direct, and it has only a moderate effect on the DOS.

PBE+U, with an on-site correction potential U_d to correct the *d*-like states [58]. This approach can better localized the *d*-state character of semiconductor [61-63], actually in some cases better than HSE06, but the total energy is less accurately derived. Moreover, although the method can be applied to *s*- and *p*-orbitals to increase the gap energy, such approach can easily generate unrealistic band curvatures [64], and we do therefore only use a correction potential to localize the *d*-like states. Herein, we choose U_d(Mn) = 4.0 eV, U_d(Fe) = 4.6 eV, U_d(Ni) = 5.1 eV, and U_d(Cu) = 4 eV U_d(Zn) = 7.5 eV, according to Setyawan *et al*. [65] With the corrected potential on the *d*-like orbitals, the *d*-like energy states are corrected and the band gap is also opened moderately (typically by ~0.3 eV or less).

4.2.2 Calculations of the Optical Properties

The optical properties are discussed based on the complex dielectric function $\varepsilon(E) = \varepsilon_1(E) + i\varepsilon_2(E)$. The dielectric function measures the electric displacement field due to the presence of an electric field in a dielectric material. The dielectric function is also an important property for describing the screening of the

charges in the material near dopants, defects, and for other structural or electronic perturbations of the crystal, like when an electric magnetic field (i. e., light) is interacting with the material. The dielectric function is described as a 3-dimensional rank 2 tensor (with the components α and β), and the interband contribution to the imaginary part $\varepsilon_2(E)$ of the dielectric function can be calculated within linear respond theory in the long wave length limit ($\lambda_{\mathbf{q}} = 2\pi/\mathbf{q} \rightarrow \infty$) through [66]

$$\varepsilon_{2,\alpha\beta}(E) = \lim_{\mathbf{q}\to 0} \frac{4\pi^2 e^2}{\Omega \mathbf{q}^2} \sum_{c,v,\mathbf{k}} 2w_{\mathbf{k}} \delta(E_c(\mathbf{k}) - E_v(\mathbf{k}) - E) \times \langle u_c(\mathbf{k} + \mathbf{e}_\alpha \mathbf{q}) | u_v(\mathbf{k}) \rangle \langle u_c(\mathbf{k} + \mathbf{e}_\beta \mathbf{q}) | u_v(\mathbf{k}) \rangle^* . \quad (4.5)$$

Here, $u_v(\mathbf{k})$ and $u_c(\mathbf{k})$ are the cell periodic part of the eigenfunctions for the VB and CB states with energies $E_v(\mathbf{k})$ and $E_c(\mathbf{k})$, respectively. Ω is the volume of primitive cell, $w_{\mathbf{k}}$ is the weight of the **k**-points in the IBZ, and $\mathbf{e}_\alpha$ is the unit vector in the Cartesian coordinates *x*, *y*, and *z*. A similar, though slightly alternative way, to calculate the dielectric response utilizes the optical matrix elements [67] as in for example the WIEN2k package. Herein, indexing of the VBs is v_1, v_2, v_3, … where v_1 is the energetically topmost VB for each **k**-point, regardless if bands cross or not along the symmetry lines. Similarly, indexing of the CBs is c_1, c_2, c_3, … where c_1 is the bottommost CB for each **k**-point.

The summation over the **k**-states in Equation 4.5 is a computationally important aspect when analysing details in the dielectric spectra. In principle, a regular summation should be sufficient, but since there are as many **k**-states as there are primitive cells in the macroscopic crystal, such summation is not possible to perform. Instead one has to rely on some approximation of the summation, and in this work we use the linear tetrahedron integration approach with a finite-size **k**-mesh [68]. The dielectric response function is directly related to the joint DOS (i .*e*., the Dirac-delta function in the equation above), and the electronic band structure is therefore the main underlying property for analysing the polarization response. This is exemplified for $CuIn_{0.5}Ga_{0.5}Se_2$ in Figure 4.2, where he total $\varepsilon_2(E)$ spectrum has been decomposed into the different contributions from each VB-to-CB transitions ($v_j \rightarrow c_{j'}$) in the summation of Equation 4.5 [69]. By comparing the different VB-to-CB transitions with the electronic structure along the symmetry lines in the IBZ, one observes that the main E1 and E2 peaks at ~3 eV in the $\varepsilon_2(E)$ spectrum (thus, a strong contribution to absorption of sunlight) arises from transitions from the energetically topmost (v_1) and second topmost (v_2) VBs to the bottommost CB (c_1) at the edge of the IBZ. Transitions from the third topmost (v_3) VBs to the bottommost CB (c_1) show a clear double peak (E3 and E4) at around 3.2 and 3.7 eV. In the energy region 4–7 eV there are contributions from several VBs but also to several CBs.

[Figure 4.2 near here]

The corresponding real part $\varepsilon_1(E)$ of the dielectric function is obtained via the Kramers-Kronig transformation relation

$$\varepsilon_{1,\alpha\beta}(E) = 1 + \frac{2}{\pi} P \int_0^\infty \frac{E' \varepsilon_{2,\alpha\beta}(E')}{E'^2 - E^2 + i\eta} dE' , \quad (4.6)$$

where P is the principal value and η is a sufficiently small number, preferably infinitesimal small number but in practice it is larger than the step length of the energy mesh. The high-frequency dielectric constant ε_∞ is determined from the dielectric function at $\varepsilon_1(E = 0)$ when the electron-optical phonon coupling is excluded, and the static dielectric constant ε_0 is calculated from the Born effective charges taking into account the ionic contribution. Experimentally, the high-frequency dielectric constant ε_∞ is determined typically in the mid-gap region, that is $\varepsilon_\infty \approx \varepsilon_1(0 << E << E_g)$, which can therefore be slightly different from the theoretically determined values, especially for small gap materials and when the frequencies of the optical phonon modes are high.

The total, geometric averaged dielectric function is obtained as

$$\varepsilon(E) = \frac{\left(\varepsilon_{xx}(E) + \varepsilon_{yy}(E) + \varepsilon_{zz}(E)\right)}{3} \quad (4.7)$$

The absorption coefficient is determined directly from the complex dielectric function through the relation

$$\alpha_{\alpha\beta}(E) = \frac{\sqrt{2}E}{\hbar c} \sqrt{\frac{\left|\varepsilon_{\alpha\beta}(E)\right| - \varepsilon_{1,\alpha\beta}(E)}{2}} , \quad (4.8)$$

where c is the speed of light. Moreover, the total, geometric averaged absorption coefficient $\alpha(E)$ is obtained similar as for the dielectric function.

Even though LDA and GGA often generate very reasonable band structures, it does underestimate the gap energies by typically 50%. A constant energy shift Δ_g of the CBs can sometimes simulate the correct gap, however, for direct-gap materials with experimental gap energies of ~1.5 eV and smaller (which is often the case for solar cell materials), the underestimated gap energy can also imply an incorrect hybridization of the CB and VB states at the gap edges [64]. That will result in incorrect band dispersions of the band edges, and thus incorrect effective electron and hole masses, also when the LDA (or GGA) generate a non-zero gap. In those cases, a constant energy shift of the CBs will not improve the incorrect hybridization, and that can yield rather strange absorption spectrum. The band curvature and the effective messes can be corrected substantially

by weakening the hybridization with any gap-state correcting method, even if the correct gap energy is not achieved [64,70]. Therefore, the LDA+U (or GGA+U) method with correction of only the *d*-like states can sometimes overcome this gap problem for Cu-based chalcogenides; that is illustrated for Cu_2ZnSnS_4 in Figure 4.3. The regular PBE potential yields $E_g \sim 0.2$ eV and that can cause too large absorption coefficient in the low-energy region due to the strong VB-CB hybridization, while PBE+U (despite small gap) and HSE06 substantially improves the spectrum.

[Figure 4.3 near here]

In addition to be careful with the underestimates gap energies in LDA and GGA for solar cell materials, one also have to considered accuracy with respect to other computational parameters. Many theoretical investigation on solar cell materials prefer to utilize hybrid functionals (often HSE06) in order to achieve good band gap energies, but because hybrid functionals are both time- and memory demanding the number of **k**-points in the calculation of the dielectric function (see Equation 4.5) is often relatively small. However, we have recently demonstrated that calculations with KS-eq in the DFT, employing the tetrahedron integration method, can require a very large **k**-mesh to accurately describe details in the absorption coefficient [28]. This is demonstrated for calculation of $\varepsilon_2(E)$ in Cu_2SiS_3 in Figure 4.4. For a small k-mesh of 5×5×5 (implying $N_{\mathbf{k}} = 39$ **k**-points in the IBZ) both HSE06 and PBE+U (corrected Δ_g to HSE06's gap energy) generate similar shape of the spectrum with a slowly increasing feature above the gap energy. Increasing the **k**-mesh to 20×20×20 ($N_{\mathbf{k}} = 2112$ **k**-points) or even 30×30×30 ($N_{\mathbf{k}} = 6992$ **k**-points) the PBE+U calculations reveal detail in the optical properties that the small **k**-mesh oversee. That is, a stronger and a clearer for energies at the gap energy is seen only when using a dense **k**-mesh.

[Figure 4.4 near here]

Since it is not computationally realistic to perform HSE06 calculations with 3000 or 5000 **k**-points, we chose herein an approximated approach to both benefit from the rather accurate gap-energies from HSE06 and the possibility to use large **k**-meshes for PBE+U to reveal **k**-dependent details of the spectrum. The imaginary part of the dielectric function $\varepsilon_2(E)$ is calculated with both HSE06 and PBE+U for the same small **k**-mesh (typically 5×5×5 for a cubic primitive cell of 8 atoms), and the spectrum of PBE+U is shifted Δ_g to match the gap energy of HSE06. Then, $\varepsilon_2(E)$ is corrected with large **k**-mesh (typically 30×30×30 for a few-atom primitive unit cell) using the PBE+U:

$$\varepsilon_{2,\alpha\beta}(E) = \varepsilon_{2,\alpha\beta}(E;\ \text{HSE06 with small } \mathbf{k}\text{-mesh}) \cdot \frac{\varepsilon_{2,\alpha\beta}(E;\ \text{PBE+U}+\Delta_g \text{ with large } \mathbf{k}\text{-mesh})}{\varepsilon_{2,\alpha\beta}(E;\ \text{PBE+U}+\Delta_g \text{ with small } \mathbf{k}\text{-mesh})}. \quad (4.9)$$

In the limit where large the **k**-mesh generates equal spectra as for the small **k**-mesh, the true HSE06 spectrum is generated. Also, in the cases where PBE+U and HSE06 generate similar spectra for any **k**-mesh, the approach will of course generate the true HSE06 spectrum for large **k**-mesh.

An alternative way could have been to use a much less computationally demanding $\mathbf{k}\cdot\mathbf{p}$ method [71] (or, even better, the modified $\mathbf{k}\cdot\tilde{\mathbf{p}}$ approach [72]) to post-calculate the optical properties on a dense **k**-mesh, based on the results (i. e., the KS single-electron energies and eigenfunctions) from HSE06 with a sparse mesh. That approach is however not employed in the present work (apart from graph in Figure 4.3).

4.2.3 Modelling the Maximum Efficiency

The maximum solar cell energy conversion efficiency is defined as

$$\eta_{\max} = \frac{P_{\max-\text{out}}}{P_{\text{in}}} = \frac{J_{\text{opt}} V_{\text{opt}}}{P_{\text{sun}}} \tag{4.10}$$

where P_{in} is the Sun's total irradiance which is $P_{\text{sun}} \approx 1000$ W/m^2, and the maximum efficiency is reached for $P_{\text{max-out}} = J_{\text{opt}} \cdot V_{\text{opt}}$ where J_{opt} and V_{opt} are the current (per unit area) and the device voltage optimized for maximum power. We model the efficiency where the current J and the device voltage V are balanced within the Shockley ideal diode equation [73–75], involving current from absorption induced excitations that are reduced by recombinations:

$$J = J_{\text{sc}} - J_{\text{r}}^{0} \cdot q \cdot \left(e^{qV/k_{\text{B}}T_{\text{c}}} - 1 \right), \tag{4.11}$$

where q is here the elementary charge, k_{B} is the Boltzmann constant, and T_{c} is the device temperature, by default set to 300 K. The first term on the right hand side is the maximum short circuit current

$$J_{\text{sc}} = q \cdot \int A(E) \cdot I_{\text{sun}}(E)\, dE \tag{4.12}$$

We consider an absorption in a single-junction cell as described by the SQ theory [73], assuming air mass 1.5 solar spectral irradiance $I_{\text{sun}}(E)$ and an absorptivity

$$A(E) = 1 - e^{-2\cdot\alpha(E)\cdot d} \tag{4.13}$$

in the absorber film with thickness d. The factor 2 in the exponential arises from the assumption that the light can be either absorb from the incoming sunlight direction or also after reflected from the back surface, thus the effective layer thickness is $2d$. The second term in Equation 4.11 is the thermal recombination current J_r^0 which can involve both radiative and non-radiative recombination:

$$J_r^0 = J_{rad}^0 + J_{non\text{-}rad}^0 = J_{rad}^0 + J_{aug}^0 \quad , \tag{4.14}$$

$$J_{rad}^0 = \frac{1}{(2\pi \cdot c)^2 \hbar^3} \cdot \int A(E) \cdot \frac{E^2}{e^{E/k_B T_c} - 1} dE, \tag{4.15}$$

$$J_{aug}^0 = q \cdot C_a \cdot d \cdot n_i^2 N_A \, . \tag{4.16}$$

The radiative recombination J^0_{rad} depends on the black-body spectrum of the device. The non-radiative recombination is here included in terms of the Auger recombination J^0_{aug} for a p-type absorber, and the effect depends mainly on the intrinsic free carrier concentrations n_i and the acceptor concentration [74]. Since we analyse the maximum efficiency of the materials, recombinations via defects are not considered in this study. C_a is the total ambipolar Auger coefficient, which is rather independent of material (typically 10^{-32}–10^{-30} cm^6/s and it is in the order of 10^{-31} for indirect transition in Si and Ge and GaAs [76-79]. We want to estimate the Auger effect using an approximate model that is material independent, and we therefore set $C_a = 10^{-31}$ cm^6/s for all considered materials. The acceptor concentration is set to $N_A = 10^{16}$ cm^{-3} which is a normal doping concentration. The square of the intrinsic carrier concentration can be expressed as $n_i^2 = n_a^2 \cdot \exp(E_g/k_B T_c)$ where $n_a = 2[m_a k_B T_c/(2\pi\hbar^2)]^{3/2}$ with the effective DOS mass $m_a = [(\gamma_e^{2/3} m_e^{DOS})(\gamma_h^{2/3} m_h^{DOS})]^{1/2}$ where γ_e is the number of CBM and m_e^{DOS} is the effective DOS mass of a single CB minimum (and corresponding for the holes in the VB maximum). Again, to construct a material independent expression, we set $m_a = 1m_0$, which is a good value for indirect material like for instance Si (with six equivalent CBM) and somewhat overestimated for Ge (with three equivalent CBM). The value is however much larger than for direct materials, like GaAs and CIGS, but since the Auger effect is much weaker for these materials, using $m_a = 1m_0$ also for these direct-gap materials does not affect the results in this work.

[Figure 4.5 near here]

Within the SQ limit, an infinite thick solar cell absorber has the theoretical maximum efficiency of $\eta_{max} \approx$ 33% for a direct band-gap energy of E_g = 1.2–1.4 eV (Figure 5(a)), independent of absorber material. Since all light is absorbed in the infinite thick layer (i. e., $A(E) = 1$ in Equation 4.15), the maximum efficiency η_{max} depends only on E_g. That is, any material with proper gap energy is in this model a suitable solar cell material.

This is no longer true for solar cell structures with finite thicknesses d, where $A(E) < 1$. This is illustrate by the thickness dependent η_{max} for $CuIn_1Se_2$, $CuIn_{0.5}Ga_{0.5}Se_2$, and $CuGaSe_2$ in Figure 4.5(b). For sufficiently large d, the efficiencies are about η_{max} = 27%, 33%, and 32%, respectively, only as a consequence of the different gap energies; here, the alloy $CuIn_{0.5}Ga_{0.5}Se_2$ with E_g = 1.21 eV has largest η_{max}. However, for thinner absorber thicknesses, the efficiencies of three compounds do not exactly follow each other because the actual energy dependence of the spectra of absorption coefficients $\alpha(E)$ differ for the three compounds. Furthermore, the drop in maximum efficiency at around 500–1000 nm is rather characteristic for traditional thin-film absorbers, and the efficiency is often rather poor for d < 500 nm. Thus, in order to design materials with high efficiency for thicknesses d < 100 nm, special requests for materials with large low-energy absorption coefficient are needed.

4.3 Results and Discussion

$Cu_2ZnSn(S,Se)_4$ (i. e., CZTSSe) have attracted increasing attention as it is an indium free alternative to $Cu(In,Ga)Se_2$ for which the costly indium is an obstacle. The first CZTS based solar cell was made in 1988 by Ito and coworkers [8] followed by more efficient devices by Friedlmeier *et al.* [9] and Katagiri *et al.* [80]. Despite the promising efficiency development, even higher efficiencies are required for CZTS to be a viable alternative. Sulfur-based CZTS has a band gap energy of $E_g \approx 1.5$ eV while the gap energy of selenium based CZTSe has a gap energy of ~1.1 eV, and with Se-S alloying/grading the cell performance and the efficiency are optimized with respect to optical absorption. While ongoing extensive research on CZTSSe reveals interesting results, other Cu-based chalcogenides as alternatives to CIGS ad CZTSSe are here regarded as emerging materials. The basic crystalline structures of a variety of emerging Cu-based chalcogenides are described in Figure 4.1 and Table 4.1.

[Table 4.1 near here]

4.3.1 CZTS Cation Alloys

There is a search for alternatively alloys to CZTSSe that can both stabilize the crystalline structure with less native defects, and at the same time provide proper band-gap energy and optoelectronic properties. Alloying in order to vary the gap energy can also be used to design device structures with graded band profile of the absorber. In addition, alloying in order to increase the gap energy is a possibility to optimize the material for a top cell absorber in tandem solar cells, where the band gap energy of the top cell shall be around 2 eV. In these cases, isovalent alloying is a natural choice of alteration that often remains the crystalline structure and does not induces localized (in-gap) defect states. A potential example of alloy is to substitute cation Sn in CZTSe or CZTS with the isovalent group-IV elements Ge or Si, thus forming the $Cu_2Zn(Sn,Si/Ge)(S/Se)_4$

alloys. Incorporation of Ge or Si in CZTSSe has been suggested as one way to increase the solar cell efficiency as well as the crystalline stability of high-quality CZTSSe [14-20]. It has been shown that the presence of Ge in CZTSe (i.e., Se as anions) can tune the gap energy to be close to the optimal value of ~1.3 eV [15,17,19] with an improved stability of the absorber layer in solar cells [16]. Alloying CZTSe with Si shall require less alloying content (estimated to $x \sim 0.3$, including correction of HSE06 gap energy) to reach $E_g \approx 1.2$ eV compared with alloying with Ge which requires much larger alloying concentration ($x \sim 1$) to reach the similar gap energy. There is a lack of data regarding expected solar cell efficiency for Si alloying of CZTS and CZTSe, which may indicate lower crystalline quality due to too strong relaxation effect since Si is a much smaller atom than Sn (and Ge). Calculations done by Shu *et al.* [17] reveals that formation enthalpies of the Ge-based alloys are smaller than those of Si-based alloys, which also is confirmed by our calculated mixing energy for $x = 0.5$, obtained from the total energies

$$\Delta E_{tot}(x) = E_{tot}(x) - [(1-x)\,E_{tot}(0) + xE_{tot}(1)\,], \qquad (4.17)$$

as presented in Figure 4.6(a), upper panel. One can notice that the mixing energy for Sn-Ge alloying is roughly half of that for Sn-Si alloying, and only about 2 meV/atom. Therefore, more investigations have been presented for Sn-Ge alloying compared to Sn-Si alloying.

In Figure 4.6(a), lower panel, we present the variation of the fundamental band-gap energy E_g with respect to the alloy composition for $Cu_2Zn(Sn,Ge/si)(S/Se)_4$. HSE06 underestimate the gap energies by roughly by 0.2 eV. Overall, the results in Figure 4.6(a) agree with earlier first-principles calculations performed by Shu *et al*. All compounds have direct bang gaps, and rather similar electronic band structures. The trend is that the gap energy increases almost linearly when the Si/Ge content increases [21]; largest change in E_g is seen for the Si-based alloy as Si normally generates larger gap energies compared to both Ge and Sn. However, there is a small non-linear contribution to the variation of the gap energies, which can be described with a bowing coefficient b in the quadratic function

$$E_g(x) = (1-x)E_g(0) + xE_g(1) - b \cdot (1-x)x \qquad (4.18)$$

The fitted bowing parameters are about 0.18 eV for the $Cu_2Zn(Sn,Ge)(S/Se)_4$ alloys, and 0.65 or 0.77 eV for the $Cu_2Zn(Sn,Si)(S/Se)_4$ alloys when also considering more alloy compositions [21]. This implies that the contribution from the quadratic term is at most 0.05 and 0.19 eV for the Sn-Ge and Sn-Si alloys, respectively. The bowing parameters are about twice that of previously reported values [17], however since the bowing parameters are small the effect on the composition dependent band-gap energy is moderate. Small bowing parameter indicates good miscibility, especially for Ge-based alloys which again indicates that it is easier to obtain crystalline Sn-Ge alloying compared with corresponding Sn-Si alloying.

[Figure 4.6 near here]

Intriguingly, the gap energies for unalloyed $Cu_2ZnSi(S/Se)_4$ compounds are significantly larger than for the corresponding Si-rich alloys ($x \approx 1$) of $Cu_2Zn(Sn,Si)(S/Se)_4$. Thus, the quadratic formula to describe composition dependence of $E_g(x)$ is not valid for ($x \approx 1$); this is specific for the Si-containing alloys, and not seen for the Ge-containing alloys. The origin to this effect is that small content of Sn in the otherwise unalloyed $Cu_2ZnSi(S/Se)_4$ compounds will not form perfectly alloys properties of CBM and VBM by hybridizing with Si, and instead Sn will form more localized Sn-like defect states near the CBM [21]. It requires higher concentration of Sn (larger than ~5% or $x < 0.95$) before Sn and Si form a more unified alloy.

The calculated absorption coefficients $\alpha(E)$ for the alloys demonstrates that all compounds have rather similar optical properties apart from different gap energies; see Figure 4.6(b). The high-frequency dielectric constants ε_∞ follows the trend that larger energy gap implies smaller dielectric constant. Especially Si-based quaternaries have large E_g and small ε_∞. However the differences in the dielectric constants between the alloys are relatively small. The difference in the static and high frequency constant is $\varepsilon_0 - \varepsilon_\infty \approx 3$, which indicates a moderate and a comparable iconicity for all compounds.

The results from these studies suggest that cation Sn-Ge alloying $Cu_2Zn(Sn,Ge)Se_4$ can be utilized to optimize the gap energy of $E_g \approx 1.3$ eV for thin-film technologies, but the theoretical analysis indicates that effect is small for Ge alloying and Si alloying may induces more defects. Furthermore, anion alloying of $Cu_2ZnSi(S,Se)_4$ is probably to prefer for optimizing gap energy to ~2 eV for a top cell material in tandem structures.

4.3.2 CZTS-like Compounds

For many of the Cu-based chalcogenides, the copper vacancy V_{Cu}^- is a shallow native acceptor with very low formation energy, and in Cu poor films vacancies can easily be formed in high concentration together with the compensated single-donor. In CZTSSe, the most prominent single donor (together with copper interstitial Cu_i^+) is the cation antisite Zn_{Cu}^+. Thus, the compensated Cu vacancy is a two-atom complex (V_{Cu}^-+Zn_{Cu}^+) with low formation energy. In addition, anti-site defect pairs (ASPs) involving Zn_{Cu}^+ and the corresponding shallow antisite acceptors Cu_{Zn}^- can be formed without change in crystalline stoichiometry [81,82]. This ASP from cation substitution (Cu_{Zn}^-+Zn_{Cu}^+) has also low formation energy in CZTSSe, and it can appear in high concentration (in the order of percentage). It is expected that such Cu-Zn disorder induces band-gap energy fluctuations in the material [83], and it is thus important to investigate how to reduce the concentration of ASP in CZTSSe. Yuan *et al.*[84] have suggested that Zn shall be substituted by the large-size atom Cd, alternative

Cu substituted by Ag, to suppress the formation of anti-site defects. They found that while Cd_{Cu}^{+} in Cu_2CdSnS_4 had as low formation energy as Zn_{Cu}^{+} in CZTS, the corresponding anti-site Zn_{Ag}^{+} in Ag_2ZnSnS_4 had significantly much higher formation energy. Therefore, investigations of C*X*TSSe (i. e., where Zn is replaced by the element *X*) are highly relevant, both in order to understand quaternary Cu-based chalcogenides in general but also in order to develop a material that it more resistant against formation of ASPs and thereby the material will be less affected by local variations in the band-gap energy. Some of these C*X*TSSe compounds can be alternative emerging candidates as thin film PV materials. The studies are also expected to reveal fundamental understanding of synthesis processes, materials' crystal stability, as well as of the defect physics in these materials.

[Figure 4.7 near here]

The electronic properties of Cu_2XSnS_4 (C*X*TS) with *X* is a 3*d* transition metal or a group-II alkaline earth metal (herein, *X* = Mn, Fe, Ni, Be, Mg, Ca, Sr, or Ba) are rather similar to those of CZTS (Figure 4.7). The C*X*TS compounds are analysed typically for the tetragonal kesterite (KS; space group S_4^2) or stannite (ST; space group D_{2d}^{11}) crystalline structures, but when those compounds are not thermodynamic stable, other crystalline structures (e.g., trigonal phase) have been found to be energetically favourable. For Cu_2MnSnS_4, Cu_2FeSnS_4, and Cu_2NiSnS_4 with magnetic element, we have also considered ferromagnetic and different antiferromagnetic configurations, and the most stable magnetic configuration is an antiferromagnetic phase described in Ref. 85. The fundamental band-gap energy E_g of Cu_2MnSnS_4 is experimentally estimated to be between 1.18 and 1.63 eV depending on the heat treatment, and a solar cell based on Cu_2MnSnS_4 has an efficiency of 0.49% [86]. The band-gap energies of synthesized Cu_2FeSnS_4 nanocrystals, Cu_2CoSnS_4, and Cu_2NiSnS_4 nanoparticles are ~1.33 or ~1.5 eV [87,88], ~1.40 [89], and ~1.40 eV [90,91], respectively. Moreover, kesterite Cu_2MgSnS_4 nanoparticles without a secondary phase have been synthesized using a hot-injection method [92]. From GGA calculations, Wang *et al*.[93] have found that kesterite Cu_2CdSnS_4 and Cu_2HgSnS_4 are thermodynamic stable, but kesterite Cu_2MgSnS_4 and especially kesterite Cu_2CaSnS_4 are not stable. Zhong *et al*. [94] found that stannite Cu_2MgSnS_4 (and $Cu_2MgSnSe_4$) are thermodynamic stable, but, similar to Wang *et al*., that kesterite and stannite phases of Cu_2CaSnS_4 (and $Cu_2CaSnSe_4$) are unstable with respect to competing compounds. Recent developments of devices based on emerging Cu_2BaSnS_4 (or Cu_2SrSnS_4) compound and anion S/Se alloying yield in early attempts a solar cell efficiency of 1.6% [95]. Experimental and theoretical characterization reveals that these compounds with large group-II elements crystallize in trigonal or orthorhombic crystalline structure [95,96].

One can estimate the thermodynamic stability of the compounds by calculating the total energy between different crystalline configurations, in conjunction with analyses of the total energies with respect to chemical decomposition, i.e., $Cu_2XSnS_4 \rightarrow$ [2(CuS) + *X*S + SnS], [Cu_2S + *X*S + SnS_2], [Cu_2SnS_3 + *X*S], or similar

mixture of compounds. We have found [85] that the total energy differences between KS and ST phases of Cu_2XSnS_4, for X = Be, Mg, Ca, Sr, and Zn are 12, 2, 30, and 3 meV/atom, respectively. Cu_2BeSnS_4 seems to be very stable crystal with respect to decomposition. In Cu_2MgSnS_4 (and also for Cu_2ZnSnS_4) presence of secondary ST phases in the materials is possible. For Cu_2SrSnS_4 and Cu_2BaSnS_4 neither of the two tetragonal structures are thermodynamic stable, instead a trigonal structure (space group C_3^2) is more stable, respectively. Intriguingly, while the trigonal phases of Cu_2SrSnS_4 and Cu_2BaSnS_4 are stable with respect to decomposition, trigonal Cu_2CaSnS_4 is unstable. Thus, the trend for S-based compounds is that lighter group-II alkaline earth metal elements of X form tetragonal structures, somewhat heavier elements of X yields unstable crystalline structures, and heavy elements of X prefer trigonal structure. The corresponding Se-based compounds with heavy group-II elements, i. e., $Cu_2SrSnSe_4$ and $Cu_2BaSnSe_4$ are more stable in orthorhombic structure (space group C_{2v}^{16}). Here it is however worth noticing that for materials and structures that balance between being stable or not, the choice of exchange-correlation potential in the calculation can give slightly different results; our results are for HSE06 calculations. While Cu_2ZnSnS_4 crystallises in non-magnetic KS phase, compounds with X being a 3d transition metal crystallise in ST or KS phase with magnetic configuration. For Cu_2MnSnS_4, the differences in total energies between the most stable ST antiferromagnetic phase and other crystalline and magnetic configurations are between 0.3 and 4 meV/atom. The larger value is from KS ferromagnetic phase which is then rather unfavourable. For Cu_2FeSnS_4, the total energy differences between stable ST antiferromagnetic and other phases are between 1 and 2 meV/atom; here, the larger value is from the KS antiferromagnetic phase. This may indicate that paramagnetic phase can exist depending on growth conditions and temperature for Cu_2MnSnS_4 and Cu_2FeSnS_4. Cu_2NiSnS_4 has a more distinct structure, where the total energy differences between most stable KS antiferromagnetic phase and the other phases are between 6 and 100 meV/atom; this large energy difference indicates that the compound has a strong magnetic phase that governs its crystalline structure. Cu_2MnSnS_4 and Cu_2FeSnS_4 are clearly stable chalcogenides. Cu_2NiSnS_4 is theoretically also stable compound from our analysis, though the energy to decompose is smaller, and this is supported by the fact that at least nanoparticles have been synthesized [97,98].

The HSE06 band-gap energies of the most stable crystalline compounds are E_g = 1.76, 1.48, 1.84, 1.80, 1.79, 1.40, 1.71, 1.26, 1.29, and 1.48 eV for CXTS with X = Be, Mg, Ca, Sr, Ba, Mn, Fe, Ni, and Zn, respectively, as obtained from the HSE06 calculations. One can notice that $Cu_2BaSnSe_4$, (and similar compounds have similar electronic structures and DOS (Figure 4.7), and the gap energies in a rather narrow energy region of about 1.6 ± 0.3 eV. We expect that these HSE06 gap energies shall be ~0.2 eV smaller that experimental values, and the calculated energies are then in good agreement with available measured data for CXTS with X = Mg (E_g = 1.6 eV), Sr (2.1 eV), Ba (1.9 eV) Mn (1.2–1.6 eV), Fe (1.3 or 1.5 eV), Ni (1.4 eV), and Zn (1.4 eV) [86-88,90,91,95,99,100,101]. Interestingly, the trigonal compounds with heavier group-II elements (i. e., Cu_2SrSnS_4 and Cu_2BaSnS_4) have more indirect-gap character of their electronic structures, which can be advantageous for absorption but dis advantageous for device efficiency. As expected the Cu d-like states

hybridize strongly with S/Se *p*-like states in the VBs. The CB DOS of compounds with Sn as group-IV cation element exhibits a strong and rather localized Sn *s*-like band at the CBM (hybridized mainly with S/Se *sp*-like anion state). This is also observed when alloying Sn with group-IV element Ge, while corresponding Si based compounds for Si *s*-like states higher up in energy region and hybridize more with other CB states [21,36]. The CB DOS of all C*X*TS (except Cu_2NiSnS_4) are is comparable that of CZTS, at least near the CBM because it is there mainly hybridization between the Sn *s*-like and the S *p*-like states [85]. It is also noticeable that Ca and Mn *d*-like states hybridize with Sn *p*-like states in the energy range above 3 eV. The electronic structure of Cu_2NiSnS_4 is somewhat different compared to the others compounds, since its Ni *d*-like states strongly hybridize with Sn *s*-like states near CBM. That results in an indirect band gap, which in contrast to the other considered C*X*TS compounds. However, the lowest CBs is flat and the indirect band-gap energy of Cu_2NiSnS_4 is only about 10 meV smaller than the direct Γ-point gap energy.

One issue with the tradition CZTS material is that disorder from Cu-Zn ASP can introduce band-gap fluctuation if the defect concentration is high, that is, if the formation energy of the defects is sufficiently small with respect to the temperatures at device operating or at the growth. The defect formation energy of defect *D* is determined from

$$\Delta H(D) = E_{\text{tot}}(\text{C}X\text{TS}{:}D) - E_{\text{tot}}(\text{C}X\text{TS}) + \Sigma_\alpha n_\alpha \cdot \mu_\alpha \,, \qquad (4.19)$$

where E_{tot}(C*X*TS:*D*) and E_{tot}(C*X*TS) are the total energies for C*X*TS with and without the defect *D*, respectively, $n_\alpha = -1$ (+1) when one atom α is added (removed), and the chemical potential μ_α. The chemical potential is split into two terms: the total energy per atom of the solid $\mu_{\alpha,\text{sol}}$ for element α, and the remaining term $\Delta\mu_\alpha$ that can vary within an energy range depending on the external condition [102]. For simplicity we choose the α-rich conditions with $\Delta\mu_\alpha = 0$ since the focus is on ASPs for which $n_\alpha = 0$ and thereby the last term in Equation 4.19 is zero. A positive (negative) value of $\Delta H(D)$ implies an energy costs (gains) to form the defect. The formation energy of compensated Cu vacancy is known to be small [102]. Also the formation energy of the ASPs (Cu_{Zn}^{-}+Zn_{Cu}^{+}) is small, and our calculated value is 0.30 eV; see Table 4.4. Notice that the compound can contain high concentration of ASP defects, making the structure disordered, though the stoichiometry remains the same as the perfect crystalline material.

[Table 4.4 near here]

For all compounds, the V_{Cu} *a*nd Cu_X defects induce rather shallow acceptor states at the VBM, and thus the Fermi level E_F is below VBM. V_{Cu} is a very delocalized acceptor that has a minor effect on the VB states and acts almost as a hole carrier doping. The X_{Cu} defect induces shallow donor states with Fermi level in the CB, and the donor shifts the CBM energetically downwards, thus a band-gap narrowing. Both Cu_X and X_{Cu} narrow

the gap. The calculated change in the band-gap energy of CZTS in Table 4.4 is similar to what has been reported before [83,103], where the band-gap energies are reduced by ~0.1 eV for Zn_{Cu}, and increased by ~0.1 eV for V_{Cu}. From the defect formation energies, we find that all considered C*X*TS have rather similar formation energy of V_{Cu} as for CZTS in the Cu-rich limit, indicating that it is easy form non-stoichiometric materials. Moreover, the $\Delta H(D)$ of the other single point defects are relatively small (see also Ref. 81), and oppositely charged point can be compensated to form neutral complexes, like (V_{Cu}+X_{Cu}) and (Cu_X+X_{Cu}). We find that the defect formation energies of (Cu_X+X_{Cu}) is small, and for Cu_2MgSnS_4, Cu_2MnSnS_4, Cu_2FeSnS_4, and Cu_2NiSnS_4, the defect formation energies is about 0.3 eV which is similar to that for CZTS. We also confirm the earlier published results [82] that the ASP in Cu_2CdSnS_4 is as easy to be formed as in CZTS despite the larger Cd atom. However, Cu_2BeSnS_4 has a relatively high defect formation energy of 0.58 eV. One reason for the larger $\Delta H(D)$ is that the atom size of Be is much smaller than the sizes of both Cu and Sn, and the relaxation effect is therefore stronger. This increase in the energy may seem to be small, but the relative change is a factor of two and the formation energy is only ~10 times k_BT for relevant temperatures. Since the defect concentration depends exponentially on the defect formation energy, i. e., $[N(D)] \propto \exp(-\Delta H(D)/k_BT)$, small variations in $\Delta H(D)$ have a large effect on $[N(D)]$. We estimate that the defect concentration $[N(Cu_X+X_{Cu})]$ is as much as ~10^4 times lower in Cu_2BeSnS_4 than in CZTS and most of the other C*X*TS. Cu_2CaSnS_4 in its tetragonal phase has very low formation energies of the (Cu_X+X_{Cu}) defect (0.13 eV) which can indicate the instability of this phase. For the corresponding trigonal phase the corresponding defect formation energy is much larger (1.40 eV), and also the (V_{Cu}+X_{Cu}) defect has about 0.6 eV larger formation energy in the trigonal phase. This suggest that it shall be possible to grow trigonal Cu_2CaSnS_4 with much less native defects compared to the other tetragonal Cu_2XSnS_4 compounds. Moreover, also the compounds with the much larger Sr or Ba elements should discourage the formation of (Cu_X^-+X_{Cu}^+) antisite disorder, but also due to trigonal structure [96].

Since the (Cu_X+X_{Cu}) defect narrows the gap and clustering enhances this effect, non-uniform distributions or concentrations of Cu-*X* disorder may imply spatial fluctuation of the band-gap energy in the material. However, the band-gap energy can be stabilized by allowing other neutral complexes that increases the gap energy, like for instance (V_{Cu}+X_{Cu}). Here, clustering of neutral (Cu_X+X_{Cu}) with neutral (V_{Cu}+X_{Cu}) can occur due to relaxation effects and preferred octet formation, as modelled by Huang *et al.* [103]. Thus, a delicate synthesis process may form a material with spatially uniform band gap despite a huge concentration of native defects and complexes.

We can conclude that most C*X*TS compounds have low formation energy of the compensated Cu-vacancy (V_{Cu}+X_{Cu}) and the ASP (Cu_X+X_{Cu}). From this initial analysis it is seems to be very little gain regarding the native defects to develop alternative (and environmentally friendly) tetragonal C*X*TS compounds, but further analysis of energy barriers to form the defects as well as better understanding of the synthesis mechanism can

be approaches to design a material with lower concentrations of ASPs or a balance of defects that compensate the effects on the electronic structure. For tetragonal Cu_2BeSnS_4, however, the formation energy is sufficiently high, and we expect in the order of 10^4 times lower concentration of the disordering at room and operating temperatures than for the other compounds. The disadvantage of ASP involving atoms with different radii is the stronger relaxation effect that can result in a larger band-gap narrowing for a given defect concentration. Moreover, Be is a toxic element and difficult to handle in synthesis processes which makes it less favourable. C*X*TS compounds with Sr and Ba, i.e.., trigonal Cu_2BaSnS_4 and Cu_2BaSnS_4, are an interesting large-gap compounds for further developments. S/Se anion alloying can form lower energy to range E_g ≈1.5–2.1 eV, however, disorder may occur due to the orthorhombic structure for Se-rich compounds.

4.3.3 Group-II Free Compounds

Another way of avoiding formation of ASPs (Cu_{Zn}+Zn_{Cu}) and compensated Cu vacancies (V_{Cu}+Zn_{Cu}) is to design materials that exclude elements with two *sp*-like valence electrons, like the group-II elements Zn, Mg, etc. or the 3*d* transition metal Mn, Fe, etc. That is, one can for example consider ternary Cu based group-IV or group-V chalcogenides and their alloys. Then, there is no natural native single donor that bonds easily with the single acceptor.

In that perspective, monoclinic Cu_2SnS_3 (CTS) with Sn as a group-IV element is a potential emerging material. The compound has already a reasonable solar cell conversion efficiencies of 4.63% and 4.29% [27,104]. The main potential advantage of CTS over the quaternary absorbers CIGS and CZTS is a relatively broad single-phase region and a reduced fabrication complexity due to fewer chemical constituents [26]. CTS can form with different crystal structures, such as the tetragonal, cubic, monoclinic, and triclinic phases, but all the commonly observed crystal structures are based on the same zinc-blende pattern with tetrahedral coordination [105]. Similar to the traditional Cu-based chalcogenides, the Cu *d*-like states dominates the VB DOS and hybridize strongly with S/Se *p*-like there, and similar to C*X*TS the energetically lower CB region dominates of Sn s-like states that hybridize with S/Se *sp*-like states (Figure 4.7).

Intriguingly, monoclinic CTS exhibits a so-called “double absorption onset” with a first onset for photon absorption at the band-gap energy E_g = 0.90–0.93 eV and a second distinct onset at about E_g + 0.1 eV [24,27,106]. It has experimentally been demonstrated that the double onset is an intrinsic feature of CTS and it does not arise from presence of other CTS phases or other compounds [107]. However, is was puzzling that the earlier theoretical study of the electronic structure and the optical properties of intrinsic CTS did not reported such double onset [105,108-110]. It was discussed if the phenomenon was a consequence of the high concentration of defects in the CTS thin films. By combining spectroscopic ellipsometry with first-principles DFT calculations of the optical properties, we have however demonstrated [28] that the double onset originates

from direct transitions at the Γ-point from three energetically close-lying VBs to a single CB in the defect-free CTS. The double onset can be predicted by DFT calculation only when using a very dense **k**-mesh to reveal fine details in the band structure. Hence, structural imperfection, like secondary phase, is not needed to explain such absorption spectrum. With the large **k**-mesh the shape of both the real and imaginary parts of the dielectric function are improved considerable in the low energy region (i. e, below 1.5 eV). The sensitivity of the calculations is that the linear tetrahedron integration method is not sufficiently good to capture small variation in the parabolic shape of the electronic band structures. That is discussed for Cu_2SiS_3 in Figure 4.4.

In principle, this inaccuracy is an issue when analysing any absorber material with several VBs, but in most material the measurements do not reveal distinct two or several onsets. The difference for CTS is that the material has a somewhat special band structure near the band edges, especially at the VBM; see Figure 4.8. One observes that the material has a direct gap at the Γ-point. The energy state of the lowest CB is rather normal with a clear energy dispersion and the CBM has the irreducible representation Γ_1 of C_2 point group. Also the VBM energy state has Γ_1 symmetry. This describes the allowed polarization of the allowed electric dipole induced transitions for that **k**-state, considering that the *y*-direction is the crystalline symmetry rotation axis for unique axis *b*. Since the topmost VB is very flat along the (010) direction (and also along the (100) direction; not displayed), the absorption of photons can be large near the gap energy, i.e., $E_g \leq E < E_g + 0.5$ eV. Moreover, similar to CZTS the lowest CB has a strong contribution of Sn *s*-like character, while the uppermost VB has primarily Cu d_{z2}-like and S p_z-like character. Along the (010) direction ((001) direction), the CB contains also S p_y-like (S p_z-like) character. This will generate an anisotropy of the dielectric response with a strong and in-plane *z*-polarized dielectric response for $E_g \leq E < E_g + 0.15$ eV. The second uppermost VB has Γ_2 symmetry at the Γ-point with primarily Cu d_{xy}-like and S p_y-like character, while the third VB has Γ_1 symmetry with primarily Cu d_{x2-y2}-like and S p_x-like character. Of the three topmost bands it is the third VB that has most Sn *s*-like character away from the Γ-point, however the contribution is small (not displayed). Noticeable, along the (001) direction, the topmost VB (with Γ_1 symmetry at VBM) and second VB (with Γ_2 symmetry) cross about 18% away from the Γ-point, while the third VB (with Γ_1 symmetry) "interacts" and bends downwards. However, the characters of the VBs change symmetry, an effect which is typically for these types of band-band interactions. Moreover, the characters of the VB states strongly affects the optical transitions. In the top panel in Figure 4.8, we present the optical matrix elements $M^{\alpha\alpha}_{v_j \to c_1} = \left|\langle \psi_{\mathbf{k}c_1} | \hat{p}_\alpha \, \psi_{\mathbf{k}v_j} \rangle\right|^2$, describing probability for optical transitions from the VB v_j to the CB c_1. One observes that close to the Γ-point the transitions from the topmost VB (blue lines) have mainly $M^{zz}_{v_1 \to c_1}$ contribution. The other terms in the optical matrix are less than 0.03, and therefore not presented in the figure. Transitions from the second VB (red lines) have mainly $M^{yy}_{v_2 \to c_1}$ contribution, while transitions from the third VB (black lines) have mainly $M^{xx}_{v_3 \to c_1}$ contribution. It is also clear how the character of the band states affects the contribution of $M^{\alpha\alpha}_{v_j \to c_1}$ when a band crosses or interacts with another band.

[Figure 4.9 near here]

The character of the bands, and the corresponding optical matrix elements, is the origin to the anisotropy of the dielectric function $\varepsilon_2(E)$ spectrum, see Figure 4.9. The computed dielectric response spectra are in good agreement with the experimental spectra from monoclinic CTS in the whole energy region 0 to 6 eV [28]. In the very low energy region ($E_g \leq E < E_g + 0.15$ eV) the polarization in the z-direction is completely dominating, while for higher photon energies also the polarization in the y-direction (and partly the x-direction) contributes to the dielectric response. The gap energy between VBM (i. e., v_1) and CBM (c_1) is directly associated to the first absorption onset at around 0.9–1.0 eV. The second the third uppermost valence bands (v_2 and v_3) have maxima also at the Γ-point, with the energies 0.12 and 0.16 eV below the VBM. These two bands are thus responsible for the second onset about 0.15 eV above the gap energy in the dielectric function $\varepsilon_2(E)$ spectrum. The three Γ-point transition energies are thus $E_A = E_g$ (equal to 0.83 eV in the HSE06 calculation), $E_B = E_g + 0.12$ eV (or 0.95 eV), and $E_C = E_g + 0.16$ eV (or 0.99 eV). The energy split of the VBs near the VBM in conjunction with the anisotropic optical matrix elements explain why monoclinic CTS exhibits so clear double onset phenomenon. In principle there is are three onset to absorption, but the E_B and E_C are (almost) undistinguishable. One notices further that the topmost VB is very flat along the (010) direction and the direct energy gap at the Y-point is only 1.70 eV = E_g + 0.93 eV. The corresponding energy at the A-point is 2.47 eV. Optical transitions at these **k**-states generates the peaks in the dielectric function for energies 1.8 to 2.5 eV, however, also **k**-states in other directions in the IBZ contributes to the spectrum in this energy range. For instance, the energy between the VBM and the second lowest CB is only 1.90 eV at the Γ-point.

Due to the sensitivity of optical response for energies closely above gap energy, we utilize the approach in Eq. 4.9 to generate the dielectric functions with a dense **k**-mesh. We present the results of the total average $\varepsilon(E) = \varepsilon_1(E) + i\varepsilon_2(E)$ for several Cu based chalcogenides in Figure 4.10. The corresponding dielectric constants are presented in Table 4.2, which can be compared with dielectric constants for traditional thin-film materials CIGS, CdTe and GaAs and also with other selected materials in Table 4.3. The related refractive index is a material property that needs to be considered when designing device with these compounds.

Overall, the difference compounds have fairly similar spectra. Binary Cu_2O is a wide gap material and can therefore be expected to have small high-frequency dielectric constant, but the data ($\varepsilon_\infty \approx 5.6$) is not significantly smaller than many other compounds ($\varepsilon_\infty \approx$ 6–8 for C*X*TS and C*X*TSe) with much smaller gap. This establishes that Cu_2O is an interesting wide-gap solar cell material for top cell structure. Moreover, the spectra of CIGS, C*X*TS, and C*X*TSe (Figure 4.10(a) and Figure 4.10(b)) are all comparable and the main

difference is the onset to response, i.e., the optical gap energy. The peak in $\varepsilon_2(E)$ in the energy region 2–4 eV follows roughly the gap energy: $Cu_2ZnSnSe_4$ has large ε_∞ = 7.7 as having small gap E_g = 0.90 eV, while Cu_2SiSnS_4 has small ε_∞ = 5.6 as having large gap E_g = 2.89 eV. The dielectric response of Cu_2NiSnS_4 deviates slightly from the other spectra as it has very strong Ni *d*-like states at the CBM. This enhances the response with a large dielectric constant of $\varepsilon_\infty \approx 7.0$. However Cu_2NiSnS_4 has small and indirect gap which is disadvantageously. The dielectric function of CTS (in Figure 4.10(c)) is $\varepsilon_\infty \approx 7.4$ for E_g = 0.83 eV, which is similar to that for $Cu_2ZnSnSe_4$; also their spectra of $\varepsilon_2(E)$ in the energy region 2–3 eV are similar. The electron optical phonon interaction effect the dielectric function in the very low energy region, typically below 0.2 eV. For the CIGS, C*X*TS, and C*X*TSe compounds, as well as CTS, the static dielectric constant increases by about 2–3 to a value of about $\varepsilon_0 \approx$ 9–12. The calculates dielectric constants normally agree rather well with the experimental data, at least considering the accuracy of theoretical determined gap energies and the measurements approach for various qualities of the materials.

[Figure 4.10 near here]

Because the band gap energy of CTS is rather small (~0.9 eV) alternative ternary chalcogenides Cu_2XS_3 (where *X* = Sn, Ge, and Si) and their cation alloys have been suggested. An option can be also with anion S-O alloying, but since oxygen has rather different atomic radius and electronegativity compared to sulphur, this is expected to be less thermodynamically advantageously. Instead, since Ge and Si are group-IV elements as Sn, it is expected to tailor the band-gap energies by alloying Sn in CTS by Ge or Si. By alloying Sn with Ge, Umehara *et al*. fabricated a solar cell using graded $Cu_2Sn_{1-x}Ge_xS_3$, with a gap energy of ~1.0 eV, and the cell efficiency of 6.7% was reported [35]. Araki *et al*. synthesized a solar cell using Cu_2GeS_3 (CGS) as an absorber, which has an efficiency of 1.70%, and the gap of CGS is between 1.5 and 1.6 eV [111]. The band-gap energy of Cu_2SiS_3 is as high as 2.56 eV, but alloying Sn with Si the band-gap energy of $Cu_2Sn_{0.5}Si_{0.5}S_3$ decreases to 1.40 eV according to measurements by Toyonaga *et al*. [112]. To our knowledge, there is no PV cell fabricated based on compounds alloying Sn with Si in CTS.

Very similar to group-IV alloying of kesterite CZTS, we find that the compounds $Cu_2Sn_{1-x}Ge_xS_3$ = $Cu_2(Sn,Ge)S_3$ and $Cu_2Sn_{1-x}Si_xS_3$ = $Cu_2(Sn,Si)S_3$ with x = 0, 0.5, and 1 have overall rather similar band dispersion and PDOS, especially near the VBM [36]; see Figure 4.7. The calculations demonstrate also that all alloys have fairly similar absorption coefficients apart from a shift in the onset energy. With Ge alloying the band-gap energy can be increased linearly by ~0.6 eV, and with Si alloying the gap energy can be increased as much as by ~1.8 eV. Overall, the trend of the calculated gap energies is rather comparable to the one from experimental measurements by Toyonaga *et al*., Umehara *et al*., and Araki *et al*. [35,111,112]. Similar to CZTS, at very high concentration of Si the alloy exhibits an abrupt increase of the gap energy. For the $Cu_2(Sn,Ge)S_3$ alloy, near the CBM the Sn or/and Ge *s*-like states mainly hybridize with S *p*-like states. For

compounds of $Cu_2(Sn,Si)S_3$ (x = 0, 0.5, and 1), Sn and Si *s*-like states of $Cu_2Sn_{0.5}Si_{0.5}S_3$ are not obviously mixed as Sn and Ge *s*-like states in $Cu_2Sn_{0.5}Ge_{0.5}S_3$, but a hybridization with S *p*-like states is found. This weaker hybridization between the Sn- and Si-orbitals can explain the non-linear increase of gap energy for high Si concentration, and it may also indicate some difficulties to form thermodynamically stable Sn-Si alloys. Furthermore, we find that for all these compounds the effective electron masses are small and apparently isotropic. The mass values are all between (0.15–0.25)m_0 in the (010) direction and between (0.13–0.22)m_0 in the (001) direction [36]; thus, the masses are thus comparable to the electron mass of CZTS ($m_e \approx 0.18m_0$) [10]. The trend is that the alloys with larger band gap have somewhat larger effective electron mass, which is consistent with the CIGS and CZTSSe [8,10]. The effective hole masses of topmost VBs are strong anisotropic in the two directions. For instance, the hole mass in CTS is 1.85m_0 in (010) direction, but 0.11m_0 in (001) direction [36]. The larger hole mass can imply that the compounds have a better electron mobility than hole mobility. The effective electron and masses were determined directly from the curvature of the energy bands through

$$m(\mathbf{k})_{\alpha\beta} = \pm \frac{\hbar^2}{\partial^2 E_j(\mathbf{k}) / \partial k_\alpha \partial k_\beta} \tag{4.20}$$

where the plus/minus sign is associated with the electrons and holes, respectively.

The Cu-group-IV chalcogenides can also be form the $Cu_4(Sn/Ge/Si)(S/Se)_4$ stoichiometry, which is then Cu and S/Se rich (or Sn/Ge/Si poor). Overall the DOS of these phases agree with their corresponding $Cu_2(Sn/Ge/Si)S_3$ compounds (not presented in figures). For example, efforts have been paid to the monoclinic and orthorhombic phase Cu_4SnS_4 for thermoelectric devices and photovoltaic applications [32,113-116]. High-quality thin film can be prepared by for example, annealing chemical bath-deposited onto chemically cleaned soda-lime glass substrates high-quality Cu4SnS4 thin [33], but the earlier calculated gap energy is rather small and direct: ~0.49 eV for orthorhombic phase [32]. This is close to our calculated indirect gap energy $E_g \approx 0.42$ eV, and with a direct Γ-point gap energy of 0.52 eV orthorhombic Cu_4SnS_4. Thus, the Sn-poor Cu_4SnS_4 composition has a considerably smaller gap energy than the Cu_2SnS_3 composition. Early measurements yielded band gap energies as high as 1.2–1.8 eV [117-119], however, diffuse reflectance data by Choudhury *et al.* [32] and spectral transmittance curves by Chalapathi *et al.* [33] indicate that the direct optical band gap of thin films was 0.92 or 1.0 eV for orthorhombic structure. Thus, further investigations are needed to establish the optoelectronic properties of this composition. Nonetheless, we find that the gap increase to ~1.10 eV for Cu_4GeS_4 and to 1.82 eV for Cu_4SiS_4, and the trend is that these materials have indirect gaps and the band gap energies are smaller than the $Cu_2(Sn/Ge/Si)S_3$ composition. The Se-based compound of Cu_2SiSe_3 decreases the gap energy by ~0.2 eV to 0.65 eV, still the material is indirect gap type.

The optical properties in terms of the dielectric functions for the compounds $Cu_2(Sn/Ge/Si)(S/Se)_3$ and $Cu_4(Sn/Ge/Si)(S/Se)_4$ are presented in Figure 4.10(c). One can observe that the materials range over a large energy region for onset E_g, and thus also the high-frequency dielectric constants varies largely ($\varepsilon_\infty \approx 6–10$)

$CuSbS_2$ (CSS) and $CuSbSe_2$ (CSSe) as well as $CuBiS_2$ (CBS) and $CuBiSe_2$ (CBSe) with the group-V element Sb or Bi are interesting alternatives to the CTS-based compounds to be potential Cu-based chalcogenides free of group-II elements. The compounds can be crystallized in an orthorhombic layered structure with composition $CuBiS_2$, but also in an orthorhombic composition Cu_3BiS_3 which is somewhat Bi poor. CBS and CSS have particularly strong absorption coefficients near the gap energy [38-40,43,45,50], which can make them of special importance for ultrathin inorganic solar cells [45]. The experimental values of the band-gaps energies for CSS, CSSe, and CBS are ~1.5 eV [42], ~1.09 eV [120] and ~1.65 eV [37], respectively. No experimental gap is available for CBSe, but earlier calculated gap energy is ~1.1 eV [50, 121]. Calculations estimates [45] that all considered compounds have indirect gaps, and the fundamental gap energies are for CSS, CSSe, CBS, and CBSe are E_g = 1.25, 0.97, 1.35, and 1.12 eV, respectively. The direct gap energies is about 0.05–0.25 eV larger. Thus, utilizing Sb or Bi as cation element implies fairly similar gap energies (slightly smaller for Bi based compounds), while utilizing Se as anion element yields some 0.3–0.4 eV smaller gap compared to that for S. Thus, this is in contrast to Ge or Sn cation alloying in CTS that more strongly affects the gap energies, but it is similar to (although slightly smaller than) effect due to S/Se anion alloying in other Cu-based chalcogenides. The solar cell energy conversion efficiency is η = 3% for devices based on $CuSbS_2$ or $CuSbSe_2$ [122,123]. In addition, the Bi poor phase Cu_3BiS_3 can be prepared by chemical bath deposition, sputtering, co-evaporation, or sulfurization of Bi-Cu metal precursors, and the reported measured band-gap energy ranges from 1.0 to 1.6 eV [46-49]. Theoretically, the band-gap energy is indirect with E_g = 1.75 eV, but the direct gap energy is only ~0.1 eV larger [50]. In contrast to the $Cu(Sb/Bi)S_2$ compounds, replacing Bi with Sb in the $Cu_3(Bi/Sb)S_3$ phases increases the gap energy, here as much as 0.3 eV. Thus, Cu_3SbS_3 compound can be utilized as wide-gap materials with $E_g \approx 2$ eV. The Se-based compound has a gap energy of ~ Cu_3SbSe_3 has a 0.2 eV smaller gap energy than it S-based compound.

Also for CSS, CSSe, CBS, and CBSe, chalcogenide alloying can be utilized to optimize and fine-tune the gap energy. Since CSSe has somewhat large gap, we also explore alloys with Te. The calculated fundamental gap energies are 0.63 eV for $CuSbTe_2$ (CSTe) and 1.12 eV for $CuBiTe_2$ (CBTe), and the direct gap energies are about 0.2–0.3 eV larger than their indirect gaps, which is then disadvantageous compared to $Cu(Sb/Bi)Se_2$. We have found that the band gap energies (similar to other chalcogenide anion alloying) follows roughly linearly with the alloy composition [45]. In $CuSb(Se,Te)_2$ the direct gap at the Γ-point $E_{g,\Gamma}$ is about 0.4 eV larger than the indirect gap $E_{g,ind}$, while the corresponding energy difference is about 0.7 eV in $CuBi(S,Se)_2$. In both the $CuSb(Se,Te)_2$ alloys and the $CuBi(S,Se)_2$ alloys, the direct $E_{g,dir}$ gap energy is only ~0.2 eV larger

than the fundamental indirect E_g. This is a rather small energy difference, and that is important for enabling efficient photovoltaics. However, an indirect gap material is known to suffer from strong Auger effect. The direct gap governs the sunlight absorption and mainly also the radiative recombination, while the indirect gap governs the Auger non-radiative recombination. Therefore, optimizing the direct-gap energy by forming bands with small (or negative) energy difference $\Delta_g = E_{g,ind} - E_{g,dir}$ is the route for tailor-making high-efficient solar cell materials.

For these Cu(Sb/Bi)(S/Se/Te)$_2$ compounds the electronic band structures of these compounds exhibit strikingly flat energy dispersions for both the CBs and VBs [45]. In contrast to compounds containing group-IV elements Sn and Ge with *s*-like CB character, the Cu-Sb/Bi chalcogenides does not generate a strong group-V *s*-like DOS peak at the lower energy region of the CB DOS; see Figure 4.7. Instead he CBs are dominated by relatively localized Sb/Bi *p*-like states and that generates a strong DOS close to the CB edges. This effect yields rather flat lowest CBs. Flat energy dispersion can imply large effective masses which can be disadvantageous for the lifetime of the carries. However, the effective electron masses at the CBM are relatively small for these compounds, for instance: $m_x \approx 0.23m_0$, $m_y \approx 0.16m_0$, and $m_z \approx 0.40m_0$ for CSTe$_2$, and $m_x \approx 0.19m_0$, $m_y \approx 0.83m_0$, and $m_z \approx 0.50m_0$ for CBSe$_2$. These values are comparable to the corresponding calculated effective masses for CIGS (~$0.1m_0$) and Si ($m_x = m_y \approx 0.2m_0$; $m_z \approx 1.0m_0$), while considerably larger than that of GaAs (~$0.08m_0$) [64,70,124]. It is worth mentioning that the mass values are valued only in the vicinity of the CBM where the band is parabolic (at most 50 meV above CBM in these materials). However, even with small effective electron mass of ~$0.1m_0$ the quasi-Fermi level is only ~20 meV above the CBM even for a high free electron concentration of 10^{17} cm^{-3} [125]. Furthermore, similar to traditional CIGS and CZTS, the VBs in these Cu-(Sb/Bi) chalcopyrites have the characteristic Cu-*d*–anion-*p* hybridization that helps forming localized band structures near the VB edges.

Since the topmost VBs are flat, also the DOS near the VB edges are strong if one compare with the DOS of CIGS and CZTSSe. Thus, the CuSb(Se,Te)$_2$ and CuBi(S,Se)$_2$ compounds have both flat CBs and VBs, and that is an advantage since it can imply a strong onset of the optical response. This is demonstrated in Figure 4.10(d) where the imaginary part $\varepsilon_2(E)$ of the dielectric function is considerable larger than that for the other compounds, especially for low energies near the gap energy E_g. Since $\varepsilon_2(E)$ is large for a wide energy range up to 5–6 eV, also the real part $\varepsilon_1(E)$ becomes large. That is reflected in the high-frequency dielectric constant. While that constant ranges $\varepsilon_\infty \approx$ 6–8 in the C*X*TZ compounds, and $\varepsilon_\infty \approx$ 6–10 in the Cu-group-IV chalcogenides, the values for the Cu-group-V chalcogenides are in the range $\varepsilon_\infty \approx$ 7–12 (and ~16 for the small-gap CuBiTe$_2$). If one compare compounds with similar band gap energies ($E_g \approx 1.3$ eV) it becomes more evident: CIGS ε_∞ = 7.1 for CIGS, 6.3 for CZTS, 7.1 for Cu$_2$(Sn,Ge)S$_3$, whereas ε_∞ = 9.4 for CBS which is close to the value for GaAs. Noticeable is also that Cu(Sb/Bi)(S/Se/Te)$_2$ have much larger and more anisotropic static dielectric function, and some compounds becomes high-κ materials. This indicates a strong ionic character of the materials, but also that the materials might be less thermodynamic stable.

4.3.4 Absorption Coefficient and Theoretical Maximum Device Efficiency

The absorption coefficient $\alpha(E)$ is determined directly from the dielectric function through Equation 4.8. One can therefore expect that Cu-group-IV chalcogenides will have slightly larger absorption than C*X*TS compounds in the low-energy region, and that Cu-group-V chalcogenides will have even larger absorption. Indeed, the absorption coefficients for the $Cu(Sb(Bi)(S/Se/Te)_2$ compounds are significantly larger than corresponding calculated results for the traditional absorbers CIGS and CZTS; see Figure 4.11. This larger $\alpha(\omega)$ is especially notable in the energy region E_g to E_g + 1.5 eV. For instance, at the photon energy $\hbar\omega = E_g$ + 1 eV, the CSSe and CBS have ~7 times larger absorption coefficients than those of CIGS and CZTS. That is a significant increase of the optical properties. The $CuSbTe_2$ compound has very good onset to absorption, however the materials has a small indirect gap ($E_{g,ind}$ = 0.63 eV) with a relatively large direct gap $\Delta_g = E_{g,ind} - E_{g,dir} \approx 0.3$ eV which is a disadvantage for the performance as a solar cell material. All materials reach $\alpha(E) = 10^5$/cm for an energy less than ~2 eV above the band gap energy. The commercialized CIGS does not have specifically large absorption coefficient, CZTS has slightly larger in the low energy region, and this demonstrate that optical properties is only one of several material properties required; crystalline quality/stability, defect physics, carrier mobility, as well as band alignment and interface physics play also important role.

[Figure 4.11 near here]

From the absorption coefficients and the gap energies, the theoretical maximum device efficiency for the absorber material within the SQ model. Since $\alpha(E)$ has the unit 1/cm, the thickness of the material determine how much of the light that is absorbed, and we therefore determine the efficiency for film thickness d; see Section 4.2.3. The maximum efficiency η_{max} for different film thicknesses d < 1000 nm is displayed in Figure. 4.12. We also compare corresponding results for traditional or other selected thin-film materials (Figure 4.12(e)). For thicknesses larger than ~1000 nm, most absorbers have sufficiently good efficiency. If the thickness increases to even further (i.e., $d \rightarrow \infty$) then η_{max} will become independent of the absorption coefficient, and it will only depend on the gap energy with $\eta_{max} \approx$ (32–34)% for CIGS, CZTSSe, CdTe, and GaAs. For the C*X*TS compounds, and CZTS and especially Cu_2MnSnS_4 exhibit very good optoelectronic properties. Cu_2O has a very good absorption coefficient, but because the band gap energy is large (E_g = 2.06 eV) the maximum efficiency is poor ($\eta_{max} \approx$ 15% for d = 2000 nm). Cu_2ZnGeS_4 (also with E_g = 2.08 eV) is a better wide-gap materials for top-cell thin-film technologies with $\eta_{max} \approx$ 20% for d = 2000 nm. Also,

$Cu_2BaSn(S/Se)_4$ has too large gap energies to be interesting for regular solar cells, but $Cu_2(Ba/Sr)SnS_4$ (with $E_g \approx 1.8$ eV with HSE06 and ~2.0 eV experimentally) is potentially interested as top-cell material as $\eta_{max} \approx$ 26% for $d = 2000$ nm.

One observes that GaAs loses much efficiency when thickness becomes smaller, and CdTe shows a typical drop in the efficiency for $d < 500$ nm. This efficiency drop is true also for CIGS and CZTS, but also for the C*X*TS compounds and the Cu-group-IV chalcogenides. For thicknesses less than 100 nm, the efficiency is less than 20% for these compounds. In order to remain its efficiency for thinner film, it is important to have strong absorption coefficient in the low energy region. That is the case for the Cu-group-V chalcogenides in Figure 4.11(d). With flat uppermost VBs, but especially with flat bottommost CBs with multi-valley structure, these materials have the potential to be high efficient also for ultrathin films. The issue with this family of compounds and their alloys is that they are indirect gap materials and the Auger effect decreases their efficiencies by about 1–5%. This decrease due to the non-radiative recombination effect is fairly constant with respect to thickness *d*, and therefore the Auger effect is less dominant for smaller thicknesses where instead the efficiency drop is due to the lower absorptivity. That is, for thin films with $d < 500$ nm, the absorption coefficient in the low photon-energy region (E_g to about $E_g + 1$ eV) is the important material property for retaining a high efficiency. Especially, the CSSe, CBS, and CBSe keep their efficiencies when the film thickness narrows down to some 100 nm. Here, CBS has a too large gap energy ($E_{g,dir} = 1.6$ eV), and its efficiency is significantly lower than the other alloy compounds, but CSSe and CBSe have more suitable gap energies and the efficiencies are close to 25% down to 100–200 nm. Further, the excellent optical properties of the CSSe and CBSe yield remarkable high efficiency even for $d = 50$–100 nm, with $\eta_{max} \approx 26\%$ for $d = 200$ nm and $\eta_{max} = 19\%$ for $d = 50$ nm. One reason for the high efficiencies for these materials is that the energy difference $\Delta_g = E_g - E_{g,dir}$ is small, only 0.06 eV for CBSe. The efficiency would have been even much larger if the energy difference $\Delta_g = E_g - E_{g,dir}$ is decreased; this is discussed in Reference 45. The Auger effect is very small if $\Delta_g = 0$ since it is suppressed by the radiative recombination that determine the voltage drop. Then the maximum efficiency increases and reaching the efficiency very close to having no Auger effect. It also means that the result is sensitive to accuracy in calculating details in the band curvatures, but also that the performance of the materials can more easily depend on crystalline quality. In Figure 4.12(f) the efficiency is presented if Auger effect is included (solid lines) or excluded (dotted lines, with same colours as for the full calculation). The effect depend strongly on Δ_g and the maximum efficiency is increases typically by some 3–5% when having no Auger effect. However, for CSSe with $\Delta_g = 0.08$ eV the Auger effect is less than 1% for thin films (and the effect is negligible in Cu_2SrSnS_4 with $\Delta_g = 0.01$ eV). Further, as an alternative the Auger recombination can be reduced by minimizing the carrier concentration since $J^0_{aug} \propto n_i^2 N_A$. That can be achieved by using materials with large fundamental gap, but too large gap will be a disadvantage for the optical absorption. For *p*-type material, the efficiency is increased by ~(1−2)% if the doping concentration decreases to $N_A = 10^{15}$ cm^{-3}. However, for intrinsic materials, the Auger model becomes $J^0_{aug} \propto n_i^2 p$ that

depends even stronger on Δ_g and on the voltage drop, and this can result in even smaller efficiency [126]. Alternatively, the carrier concentration can be decreased by smaller effective DOS masses [45]. The employed effective DOS mass in this work is $m_a = 1m_0$ which is estimated to be somewhat too large, especially for CSTe. If one instead using a smaller mass of $m_a = 0.4m_0$ (and with $\Delta_g \approx$ 0.2 eV) the maximum efficiency of $CSTe_2$ increases by ~1.5%. However, trying to optimize the electronic band structure to obtain even smaller DOS masses also means more dispersion of the band structure and thereby smaller absorption coefficient. Therefore, multi-valley engineering [to achieve large joint DOS and large $\alpha(\omega)$] balanced with band-edge engineering for small effective masses (with low carrier concentration $n_i^2 \propto [(\gamma_e^{2/3} m_e^{DOS}) \cdot (\gamma_h^{2/3} m_h^{DOS})]^{3/2}$ and long lifetime) is the concept to tailor-make materials for even thinner solar cells. Here, better models that include non-parabolic energy dispersion together with better description for the absorption/recombination are required for more accurate describing the material behaviour. Furthermore, similar to the other chalcogenides, anion alloying can tune in the gap energy for a maximum efficiency, but the alloying have almost no impact on the energy difference Δ_g. There are also other emerging solar cell materials that have high efficiency for d < 100 nm, and especially $BaSi_2$ shall be mentioned here which has suitable gap energy and sufficiently small Δ_g. Its electronic properties and defect physics have theoretically been explored by Kumar *et al.* [127].

The overall results demonstrate that Cu-group-V chalcogenides, e.g. the $CuSb(Se,Te)_2$ and $CuBi(S,Se)_2$ alloys with optimized E_g, that there are alternative emerging Cu-based chalcogenides for ultrathin inorganic photovoltaics [45]. The advantage with such thin film absorber layer is the shorter path for the minority carriers. We can thus conclude that there are several emerging Cu-based group-II-free chalcogenides that have superior optical properties over the more traditional solar cell absorbers. The compounds with group-IV Sn and especially the group-V Sb and Bi are suitable for ultrathin inorganic solar cell, and it is possible to (theoretically) achieve a single-junction solar cells with a maximum efficiency of η_{max} > 25% even for film thicknesses d < 100 nm if the Auger recombination is avoided or diminished. The challenge is of course to be able to develop and tune synthesis to fabricate materials with sufficiently good quality without devastating native defects. Nonetheless, the result can be a guidance when designing future materials for ultrathin solar cells.

[Figure 4.12 near here]

4.4 Summary

We have investigated the structural, electronic, and optical properties of several emerging copper-based

chalcogenides, employing DFT based atomistic first-principles computational methods, and compared the materials properties of these chalcogenides with traditional as well as other proposed compounds for thin-film inorganic PV applications. We have demonstrated that it is possible to develop inorganic PV with ultrathin photon-absorbing film (i. e., with thicknesses $d < 100$ nm). The material shall exhibit optimized band-gap energy E_g as well as having a very high absorption coefficient $\alpha(E)$ in the lower energy spectrum, that is, for photons with energies near the gap energy $E_g \leq E < (E_g + 2\ \text{eV})$. However, concern regarding material quality and modifications in the band dispersion is needed in order to minimize the non-radiative recombination. That is, to tailor-make materials for very thin, inorganic PV technologies one shall consider (*i*) an optimized band-gap energy for the specific film thickness. The fundamental optoelectronic performances can easily be fine-tuned by alloying with isovalent elements. In addition, we suggest that one (*ii*) designs materials with multi-valley band edges that absorbs sunlight at several valleys in the IBZ. Thus, the VBM and CBM shall be away from the Γ-point, out in the IBZ. To further enhance strong absorption in the lower energy spectrum the materials shall have (*iii*) rather flat energy dispersions to achieve high absorption coefficient for the low photon energies $E = \hbar\omega = E_g$ to $E_g + 2$ eV. Thinner films requires high absorption in an even more narrow energy region, perhaps $\hbar\omega = E_g$ to $E_g + 1$ eV. However, (*iv*) the band structure shall have direct fundamental gap to avoid Auger recombinations; thus both CBM and VBM shall then be located at the same **k**-point but away from the Γ-point. Preferable, the material shall also have (*v*) small DOS electron and hole masses reduce the intrinsic carrier concentration, which in turn reduces the Auger effect. Also, (*vi*) with small effective electronic masses the materials will exhibit high minority carrier mobility. The preferred requirements of flat band dispersion for high sunlight absorption and small mass for low band filling and high mobility are often competing characteristics, and the materials have to be fine-tuned an optimized the balance of these two characteristics. In addition to this, the material shall of course, as for regular thin-film PV, (*vii*) involve only earth abundant, non-toxic, and inexpensive elements, and the devices shall be inexpensive regarding fabrication and handling. The material must also be (*viii*) thermodynamic stable with no devastating in-gap defect states, be able to be doped, and to have suitable band alignment at the interfaces.

Acknowledgement

We thank the Research Council of Norway (projects 243642, 221469, and 251131) as well as the Swedish Foundation for Strategic Research for financial support. We acknowledge access to high performance computer resources at University of Oslo (UiO) in Norway operated by University Center for Information Technology (USIT) provided through National infrastructure for high-performance computing (NOTUR), as well as at KTH Royal Institute of Technology in Stockholm, operated by Center for High Performance Computing (PDC), and at Linköping University also in Sweden, operated by National Supercomputer Centre (NSC), through Swedish National Infrastructure for Computing (SNIC). We also acknowledge the Partnership for Advanced Computing in Europe (PRACE) for awarding access to resource MareNostrum

based in Spain at the Barcelona Supercomputing Center – Centro Nacional de Supercomputación (BSC-CNS), and access to the resource Archer based in the UK Edinburgh with support from the Distributed European Computing Initiative (DECI) in PRACE aisbl. We acknowledge scientific discussions with Dr. Andrea Crovetto at Technical University of Denmark (DTU) Denmark, Dr. Sukgeun G. Choi now at University of California at Santa Barbara in USA, and teams led by Prof. Marika Edoff and Prof. Charlotte Platzer Björkman at Uppsala University in Sweden.

References

1. *International Technology Roadmap for Photovoltaic: 2017 Results*, 9th edition, ITRPV, 2018.
2. *Best Research-Cell Efficiencies, Rev. 10-30-2017*, National Renewable Energy Laboratory, Denver, 2017.
3. *Clean Electricity from Photovoltaics*, ed. M.D. Archer and R. Hill, Imperial College Press, London, 2001.
4. S. Siebentritt, M. Igalson, C. Persson and S. Lany, *Prog. Photovoltaics Res. Appl.*, 2010, **18**, 390.
5. *Handbook of Photovoltaic Science and Engineering*, ed. A. Luque and S. Hegedus, John Wiley & Sons Ltd, Chichester, 2011.
6. *Solar Cells*, 2nd edition, ed. A. McEvoy, T. Markvart and L. Castañer, Elsevier, Oxford, 2013.
7. T. Feurer, P. Reinhard, E. Avancini, B. Bissig, J. Lockinger, P. Fuchs, R. Carron, T.P. Weiss, J. Perrenoud, S. Stutterheim, S. Buecheler and A.N. Tiwari, *Prog. Photovoltaics Res. Appl.*, 2017, **25**, 645.
8. K. Ito and T. Nakazawa, *Jpn J. Appl. Phys.*, 1988, **27**, 2094.
9. T. M. Friedlmeier, N. Wieser, T. Walter, H. Dittrich and H. W. Schock, *14th Eur. Conf. PV, Bedford*, 1997, p.1242.
10. C. Persson, *J. Appl. Phys.*, 2010, **107**, 053710.
11. *Thin Film Solar Cells from Earth Abundant Materials*, ed. S. Kodigala, Elsevier, Oxford, 2013.
12. *Copper Zinc Tin Sulphide-based Thin Film Solar Cells*, ed. K. Ito, John Wiley & Sons, Ltd, Chichester, 2015.
13. S. Li, S. Zamulko, C. Persson, N. Ross, J. Larsen and C. Platzer-Bjorkman, *Appl. Phys. Lett.*, 2017, **110**, 021905.
14. G.Q. Yao, H.S. Shen, E.D. Honig, R. Kershaw, K. Dwight and A. Wold, *Solid State Ion.*, 1987, **24**, 249.
15. H.-R. Liu, S. Chen, Y.-T. Zhai, H.J. Xiang, X.G. Gong and S.-H. Wei, *J. Appl. Phys.*, 2012, **112**, 093717.
16. S. Bag, O. Gunawan, T. Gokmen, Y. Zhu and D.B. Mitzi, *Chem. Mater.*, 2012, **24**, 4588.
17. Q. Shu, J.-H. Yang, S. Chen, B. Huang, H. Xiang, X.-G. Gong and S.-H. Wei, *Phys. Rev. B*, 2013, **87**, 115208.
18. M. Hamdi, A. Lafond, C. Guillot-Deudon, F. Hlel, M. Gargouri and S. Jobic, *J. Solid State Chem.*, 2014, **220**, 232.
19. D.B. Khadka and J. Kim, *J. Phys. Chem. C*, 2015, **119**, 1706.
20. X. Zhang, D. Rao, R. Lu, K. Deng and D. Chen, *AIP Adv.*, 2015, **5**, 057111.
21. S. Zamulko, R. Chen and C. Persson, *Phys. Status Solidi B*, 2017, **254**, 1700084.
22. L. O. Grondahl, *Rev. Mod. Phys.*, 1933, **5** 141.
23. B.P. Rai, *Solar Cells*, 1988, **25**, 265.
24. D.M. Berg, R. Djemour, L. Gütay, G. Zoppi, S. Siebentritt and P. J. Dale, *Thin Solid Films*, 2012, **520**, 6291.
25. N. Aihara, A. Kanai, K. Kimura, M. Yamada, K. Toyonaga, H. Araki, A. Takeuchi and H. Katagiri, *Jpn. J. Appl. Phys.*, 2014, **53**, 5S1.
26. L.L. Baranowski, P. Zawadzki, S. Christensen, D. Nordlund, S. Lany, A.C. Tamboli, L. Gedvilas, D.S. Ginley, W. Tumas, E.S. Toberer and A. Zakutayev, *Chem. Mater.*, 2014, **26**, 4951.

27. M. Nakashima, J. Fujimoto, T. Yamaguchi and M. Izaki, *Appl. Phys. Express*, 2015, **8**, 042303.
28. A. Crovetto, R. Chen, R.B. Ettlinger, A.C. Cazzaniga, J. Schou, C. Persson and O. Hansen, *Sol. Energy Mater. Sol. Cells*, 2016, **154**, 121.
29. A.C. Lokhande, R.B.V. Chalapathy, M. He, E. Jo, M. Gang, S.A. Pawar, C.D. Lokhande and J.H. Kim, *Sol. Energy Mater. Solar Cells*, 2016, **153**, 84.
30. D. Tiwari, T. Koehler, R. Klenk and D.J. Fermin, *Sustainable Energy Fuels*, 2017, **1**, 899.
31. Q. Chen, X. Dou, Z. Li, Y. Ni, J. Chen, F. Zhou, Y. Yamaguchi and S. Zhuang, *Optik*, 2014, **125**, 3217.
32. A. Choudhury, S. Mohapatra, H. Yaghoobnejad Asl, S.H. Lee, Y.S. Hor, J.E. Medvedeva, D.L. McClane, G.E. Hilmas, M.A. McGuire, A.F. May, H. Wang, S. Dash, A. Welton, P. Boolchand, K.P. Devlin, J. Aitken, R. Herbst-Irmer and V. Petříček, *J. Solid State Chem.*, 2017, **253**, 192.
33. U. Chalapathi, B. Poornaprakash and S.-H. Park, *Sol. Energy*, 2017, **155**, 336.
34. X. Chen, M. Onoda, H. Wada, A. Sato, H. Nozaki and R. Herbst-Irmer, *J. Solid State Chem.*, 1999, **145**, 204.
35. M. Umehara, S. Tajima, Y. Aoki, Y. Takeda and T. Motohiro, *Appl. Phys. Express*, 2016, **9**, 072301.
36. R. Chen and C. Persson, *Phys. Status Solidi B*, 2017, **254**, 1700111.
37. S.H. Pawar, A.J. Pawar and P.N. Bhosale, *Bull. Mater. Sci.*, 1986, **8**, 423.
38. Y. Rodriguez-lazcano, M.T.S. Nair and P.K. Nair, *J. Cryst. Growth*, 2001, **223**, 399.
39. P.S. Sonawane, P.A. Wani, L.A. Patil and T. Seth, *Mater. Chem. Phys.*, 2004, **84**, 221.
40. J. Zhou, G.Q. Bian, Q.Y. Zhu, Y. Zhang, C.Y. Li and J. Dai, *J. Solid State Chem.*, 2009, **182**, 259.
41. A. Rabhi, M. Kanzari and B. Rezig, *Thin Solid Films* 2009, **517**, 2477.
42. D. Colombara, L.M. Peter, K.D. Rogers, J.D. Painter and S. Roncallo, *Thin Solid Films* 2011, **519**, 7438.
43. M. Kumar and C. Persson. *J. Renewable Sustainable Energy* 2013, **5**, 031616.
44. M. Kumar and C. Persson, *Energy Procedia*, 2014, **44**, 176.
45. R. Chen and C. Persson, *EPJ Photovoltaics*, 2017, **8**, 85504.
46. V. Estrella, M.T.S. Nair and P.K. Nair, *Semicond. Sci. Technol.*, 2003, **18**, 190.
47. N.J. Gerein and J.A. Haber, *Chem. Mater.*, 2006, **18,** 6297.
48. F. Mesa, A. Dussan and G. Gordillo, *Phys. Status Solidi C*, 2010, **7**, 917.
49. D. Colombara, L.M. Peter, K. Hutchings, K.D. Rogers, S. Schäfer, J.T.R. Dufton and M.S. Islam, *Thin Solid Films*, 2012, **520**, 5165.
50. M. Kumar and C. Persson, *Appl. Phys. Lett.*, 2013, **102**, 062109.
51. P. Hohenberg and W. Kohn, *Phys. Rev.*, 1964, **136**, B864.
52. W. Kohn and L.J. Sham, *Phys. Rev.*, 1965, **140**, A1133.
53. G. Kresse and J. Hafner, *Phys. Rev. B*, 1993, **47**, 558.
54. G. Kresse and D. Joubert, *Phys. Rev. B*, 1999, **59**, 1758.
55. P. Blaha, K. Schwarz, G.K.H. Madsen, D. Kvasnicka and J. Luitz, *WIEN2k, An Augmented Plane Wave + Local Orbitals Program for Calculating Crystal Properties* (Karlheinz Schwarz, Techn. Universität Wien, Austria), 2001. ISBN 3-9501031-1-2.

56. J.P. Perdew, K. Burke and M. Ernzerhof, *Phys. Rev. Lett.*, 1996, **77**, 3865.
57. J.P. Perdew, A. Ruzsinszky, G.I. Csonka, O.A. Vydrov, G.E. Scuseria, L.A. Constantin, X. Zhou and K. Burke, *Phys. Rev. Lett.*, 2008, **100**, 136406.
58. V. I. Anisimov, J. Zaanen and O. K. Andersen, *Phys. Rev. B*, 1991, **44**, 943.
59. J. Heyd, G.E. Scuseria and M. Ernzerhof, *J. Chem. Phys.*, 2003, **118**, 8207.
60. A.V. Krukau , O.A. Vydrov, A.F. Izmaylov and G.E. Scuseria, *J. Chem. Phys.*, 2006, **125**, 224106.
61. C. Persson and A. Zunger, *Appl. Phys. Lett.*, 2005, **87**, 211904.
62. C. Persson, C.L. Dong, L. Vayssieres, A. Augustsson, T. Schmitt, M. Mattesini, R. Ahuja, J. Nordgren, C.L. Chang, A. Ferreira da Silva and J.-H. Guo, *Microelectron. J.*, 2006, **37**, 686.
63. G. Baldissera and C. Persson, *J. Appl. Phys.*, 2016, **119**, 045704.
64. C. Persson and S. Mirbt, *Br. J. Phys.*, 2006, **36**, 286.
65. W. Setyawan, R.M. Gaume, S. Lam, R.S. Feigelson and S. Curtarolo, *ACS Comb. Sci.*, 2011, **13**, 382.
66. M. Gajdoš, K. Hummer, G. Kresse, J. Furthmüller and F. Bechstedt, *Phys. Rev. B*, 2006, **73**, 045112.
67. C. Ambrosch-Draxl and J.O. Sofo, *Comp. Phys. Commun.*, 2006, **175**, 1.
68. P.E. Blöchl, O. Jepsen and O.K. Andersen, *Phys. Rev. B*, 1994, **49**, 16223.
69. S.G. Choi, R. Chen, C. Persson, T.J. Kim, S.Y. Hwang, Y. D. Kim and L.M. Mansfield, *Appl. Phys. Lett*., 2012, **101**, 261903.
70. C. Persson, R. Ahuja and B. Johansson, *Phys. Rev. B*, 2001, **64**, 033201.
71. C. Persson and C. Ambrosch-Draxl, *Comp. Phys. Commun.*, 2007, **177**, 280.
72. K. Berland and C. Persson, *Comput. Mater. Sci.*, 2017, **134**, 17; ibid, *J. Appl*, *Phys.*, 2018, **123**, 205703.
73. W. Shockley and H.J. Queisser *J. Appl. Phys.*, 1961, **32**, 510.
74. A. Cuevas, *Energy Procedia*, 2014, **55**, 53.
75. K.L. Chopra and S.R. Das, *Thin Film Solar Cells*, Springer, New York, 1983.
76. S. Dominici, H. Wen, F. Bertazzi, M. Goano and E. Bellotti, *Appl. Phys. Lett.*, 2016, **108**, 211103.
77. D. Steiauf, E. Kioupakis and C.G. Van de Walle, *ACS Photonics*, 2006, **108**, 211103.
78. J. Dziewior and W. Schmid, *Appl. Phys. Lett.*, 1977, **31**, 346.
79. R.A. Sinton and R.M. Swanson, *IEEE Trans. Electron Dev.*, 1987, **ED–34**, 1380.
80. H. Katagiri, K. Saitoh, T. Washio, H. Shinohara, T. Kurumadani and S.Miyajima, *Proc of Techn. Digest 11th Int. Photovolt. Sci. Eng. Conf*., 1999, p.647.
81. S. Chen, J.-H. Yang, X.G. Gong, A. Walsh and S.-H. Wei, *Phys. Rev. B*, 2010, **81**, 245204.
82. B.G. Mendis, M.D. Shannon, M.C.J. Goodman, J.D. Major, A.A. Taylor, D.P. Halliday and K. Durose, *J. Phys. Conf. Ser.*, 2013, **471**, 012014.
83. J.J.S. Scragg, J.K. Larsen, M. Kumar, C. Persson, J. Sendler, S. Siebentritt and C. Platzer-Björkman, *Phys. Status Solidi B*, 2016, **253**, 247.
84. Z.-K. Yuan, S. Chen, H. Xiang, X.-G. Gong, A. Walsh, J.-S. Park, I. Repins and S.-H. Wei, *Adv. Funct. Mater.*, 2015, **25**, 6733.
85. R. Chen and C. Persson, *J. Appl. Phys.*, 2017, **121**, 203104.

86. L. Chen, H. Deng, J. Tao, H. Cao, L. Huang, L. Sun, P. Yang and J. Chu, *RSC Adv.*, 2015, **5**, 84295.
87. L.Li, X. Liu, J. Huang, M. Cao, S. Chen, Y. Shen and L. Wang, *Mater. Chem. Phys.*, 2012, **133**, 688.
88. X. Zhang, N. Bao, K. Ramasamy, Y.H.A. Wang, Y. Wang, B. Lin and A. Gupta, *Chem. Commun.*, 2012, **48**, 4956.
89. B. Murali, M. Madhuri and S.B. Krupanidhi, *Cryst. Growth Des.*, 2014, **14**, 3685.
90. T.-X.Wang, Y.-G. Li, H.-R. Liu, H. Li and S.-X. Chen, *Mater. Lett.*, 2014, **124**, 148.
91. A. Kamble, K. Mokurala, A. Gupta, S. Mallick and P. Bhargava, *Mater. Lett.*, 2014, **137**, 440.
92. M. Wei, Q. Du, R. Wang, G. Jiang, W. Liu and C. Zhu, *Chem. Lett.*, 2014, **43**, 1149.
93. C. Wang, S. Chen, J.H. Yang, L. Lang, H.J. Xiang, X.G. Gong, A. Walsh and S.-H. Wei, *Chem. Mater.*, 2014, **26**, 3411.
94. G. Zhong, K. Tse, Y. Zhang, X. Li, L. Huang, C. Yang, J. Zhu, Z. Zeng, Z. Zhang and X. Xiao, Thin Solid Films, 2016, **603**, 224.
95. D. Shin, B. Saparov, T. Zhu, W.P. Huhn, V. Blum and D.B. Mitzi, *Chem. Mater.*, 2016, **28**, 4771.
96. F. Hong, W. Lin, W. Meng and Y. Yan, *Phys. Chem. Chem. Phys.*, 2016, **18**, 4828.
97. T.-X.Wang, Y.-G. Li, H.-R. Liu, H. Li and S.-X. Chen, *Mater. Lett.*, 2014, **124**, 148.
98. A. Kamble, K. Mokurala, A. Gupta, S. Mallick and P. Bhargava, *Mater. Lett.*, 2014, **137**, 440.
99. M. Wei, Q. Du, R. Wang, G. Jiang, W. Liu and C. Zhu, *Chem. Lett.*, 2014, **43,** 1149.
100. P.M.P. Salomé, J. Malaquias, P.A. Fernandes, M.S. Ferreira, A.F. da Cunha, J.P. Leitão, J.C. González and F.M. Matinaga, *Sol. Energy Mater. Sol. Cells*, 2012, **101**, 147.
101. J. Llanos, C. Mujica, V. Sánchez and O. Peña, *J. Solid State Chem.*, 2003, **173**, 78.
102. C. Persson, S. Lany, Y.-J. Zhao and A. Zunger, *Phys. Rev. B*, 2005, **72**, 035211.
103. D. Huang and C. Persson, *Thin Solid Films*, 2013, **535**, 265.
104. A. Kanai, K. Toyonaga, K. Chino, H. Katagiri and H. Araki, *Jpn. J. Appl. Phys.*, 2015, **54**, 08KC06.
105. Y.-T. Zhai, S. Chen, J.-H. Yang, H.-J. Xiang, X.-G. Gong, A. Walsh, J. Kang and S.-H. Wei, *Phys. Rev. B*, 2011, **84**, 075213.
106. N. Aihara, A. Kanai, K. Kimura, M. Yamada, K. Toyonaga, H. Araki, A. Takeuchi and H. Katagiri, *Jpn. J. Appl. Phys.*, 2014, **53**, 05FW13.
107. J. de Wild, E.V.C. Robert, B. El Adib and P.J. Dale, MRS Proc., 2015, **1771**, mrss15–2135683.
108. L. Xi, Y.B. Zhang, X.Y. Shi, J. Yang, X. Shi, L.D. Chen, W.Q. Zhang, J.H. Yang and D.J. Singh, *Phys. Rev. B*, 2012, **86**, 155201.
109. P. Zawadzki, L.B. Lauryn, H.W. Peng, E.S. Toberer, D.S. Ginley, W. Tumas, Z. Andriy and S. Lany, *Appl. Phys. Lett.*, 2013, **103**, 253902.
110. A. Shigemi, T. Maeda and T. Wada, *Phys. Status Solidi b*, 2015, **252**, 1230.
111. H. Araki, K. Chino, K. Kimura, N. Aihara, K. Jimbo and H. Katagiri, *Jpn. J. Appl. Phys.*, 2014, **53**, 05FW10.
112. K. Toyonaga and H. Araki, *Phys. Status Solidi C*, 2015, **12**, 753.
113. M. Hasaka, T. Aki, T. Morimura and S.-I. Kondo, *Energ. Convers. Manag.*, 1997, **38**, 855.

114. M.I. Aliev, D.G. Arasly and T.G. Dzhabrailov, *Sov. Phys. Solid State,* 1983, **25**, 2009.
115. Y. Goto, Y. Kamihara and M. Matoba, *J. Electron Mater.*, 2014, **43**, 2202.
116. A. Suzumura, N. Nagasako, Y. Kinoshita, M. Watanabe, T. Kita and R. Asahi, *Mater. Trans.*, 2015, **56**, 858.
117. K. Anuar, S. M. Ho, W.T. Tan, M.S. Atan, D. Kuang, H. Jelas and N. Saravanan, *Mater. Sci.*, 2008, **14**, 101.
118. A. Kassim, Z. Kuang, A. Sharif, T. Wee, H.S. Min and S. Nagalingam, *Arab. J. Sci. Eng.*, 2010, **35**, 83.
119. D. Avellaneda, M.T.S. Nair and P.K. Nair, *J. Electrochem. Soc.*, 2010, **157**, D346.
120. D. Tang, J. Yang, F. Liu, Y. Lai, J. Li and Y. Liu, *Electrochim. Acta,* 2012, **76**, 480.
121. D.J. Temple, A.B. Kehoe, J.P. Allen, G.W. Watson and D.O. Scanlon, *J. Phys. Chem. C,* 2012, **116**, 7334.
122. W. Septina, S. Ikeda, Y. Iga, T. Harada and M. Matsumura, *Thin Solid Films,* 2014, **550**, 700.
123. A.W. Welch, L.L. Baranowski, P. Zawadzki, S. Lany, C.A. Wolden and A. Zakutayev, *Appl. Phys. Express*, 2015, **8**, 082301.
124. C. Persson, *App. Phys. Lett.*, 2008, **93**, 072106.
125. R. Chen and C. Persson, *J. Appl. Phys.*, 2012, **112**, 103708.
126. A. Cuevas, *Energy Procedia,* 2014, **55**, 53.
127. M. Kumar, N. Umezawa and M. Imai, *Appl. Phys. Express*, 2014, **7**, 071203.

Table 4.1 Crystal structure parameters of the considered copper-based chalcogenides: space group names, lattice parameters (*a*, *b*, *c*, and non-trivial β angle) and cation-anion bond lengths δ(cation *X*–anion), as obtained from the calculations with the HSE06 exchange-correlation potential. The Cu_2XSnS_4 (*X* = Mn, Fe and Ni) compounds have antiferromagnetic configuration that slightly distort the crystalline structure.

Compound	*Space group*	*a [Å]*	*b [Å]*	*c [Å] β [°]*	*Bond lengths δ(X–*anion*) [Å]*
$CuGaSe_2$	D_{2d}^{12}; 122	5.610	5.610	11.000	Cu: 2.42; Ga: 2.41
$CuInSe_2$	D_{2d}^{12}; 122	5.833	5.833	11.649	Cu: 2.42; In: 2.59
$Cu_2ZnSnSe_4$	S_4^2; 82	5.740	5.740	11.380	Cu: 2.45; Zn: 2.47; Sn: 2.55
Cu_2ZnSnS_4	S_4^2; 82	5.457	5.457	10.827	Cu: 2.33; Zn: 2.35; Sn: 2.41
Cu_2ZnGeS_4	S_4^2; 82	5.355	5.355	10.512	Cu:2.33; Zn: 2.34; Ge: 2.23
Cu_2ZnSiS_4	S_4^2; 82	5.307	5.307	10.625	Cu: 2.35; Zn: 2.36; Si: 2.15
Cu_2CdSnS_4	D_{2d}^{11}; 121	5.622	5.622	10.819	Cu: 2.34; Cd: 2.54; Sn: 2.41
Cu_2BeSnS_4	S_4^2; 82	5.263	5.263	10.373	Cu: 2.28; Be: 2.11; Sn: 2.43
Cu_2MgSnS_4	D_{2d}^{11}; 121	5.489	5.489	10.731	Cu: 2.28; Mg: 2.45; Sn: 2.44
Cu_2CaSnS_4	D_{2d}^{11}; 121	5.809	5.809	10.253	Cu: 2.32; Ca: 2.69; Sn: 2.42
	C_3^2; 144	6.304	6.304	15.631	Cu: 2.30-2.37; Sr: 3.13-3.22; Sn: 2.40
Cu_2BaSnS_4	C_3^2; 144	6.401	6.401	15.868	Cu: 2.34-2.37; Ba: 3.23-3.25; Sn: 2.40
$Cu_2SrSnSe_4$	C_{2v}^{16}; 40	11.048	10.912	6.713	Cu: 2.43-2.53; Sr: 3.23-3.33; Sn: 2.54
$Cu_2BaSnSe_4$	C_{2v}^{16}; 40	11.180	11.371	6.779	Cu: 2.45-2.52; Ba: 2.37-2.44; Sn: 2.54
Cu_2MnSnS_4	D_{2d}^{11} ; 121	5.473	5.473	10.727	Cu: 2.29; Mn: 2.44; Sn: 2.43
Cu_2FeSnS_4	D_{2d}^{11}; 121	5.432	5.432	10.603	Cu: 2.28; Fe: 2.35; Sn: 2.43
Cu_2NiSnS_4	S_4^2; 82	5.464	5.464	10.398	Cu: 2.30; Ni: 2.28; Sn: 2.45
Cu_2O	O_h^4; 224	4.237	4.237	4.237	Cu: 1.83
Cu_2SnS_3	$\boldsymbol{C_s^4}$; 9	6.664	11.574	6.682 β = 108.85	Cu: 2.31, 2.40 Sn: 2.30, 2.48
Cu_2GeS_3	C_s^4; 9	6.445	11.317	6.439 β = 108.42	Cu: 2.30, 2.37 Sn: 2.18, 2.32
Cu_2SiS_3	C_s^4; 9	6.338	11.224	6.287 β = 108.11	Cu: 2.30, 2.38 Si: 2.09, 2.22
Cu_4SnS_4	D_{2h}^{16}; 62	14.486	7.874	5.557	Cu: 2.24, 2.29, 2.39, 2.43, 2.50 Sn: 2.43, 2.47, 3.08
Cu_4GeS_4	D_{2h}^{16}; 62	14.204	7.615	5.608	Cu: 2.21, 2.25, 2.38, 2.48, 2.52 Ge: 2.22, 2.28
Cu_4SiS_4	D_{2h}^{16}; 62	14.030	7.475	5.650	Cu: 2.20, 2.23, 2.26, 2.29, 2.38, 2.48, 2.53 Si: 2.09, 2.13, 2.18
Cu_4GeSe_4	D_{2h}^{16}; 62	14.705	8.235	5.695	Cu: 2.33, 2.40, 2.45, 2.50, 2.61, 2.53, 2.66 Ge: 2.40, 2.45
Cu_4SiSe_4	D_{2h}^{16}; 62	14.591	8.061	5.784	Cu: 2.32, 2.40, 2.43, 2.36, 2.51, 2.57, 2.61, 2.73; Si: 2.26, 2.29, 2.35
Cu_3SbS_3	D_2^4; 19	8.221	10.139	6.662	Sb: 2.46; Cu: 2.26-2.33
Cu_3SbSe_3	D_2^4; 19	8.383	10.740	6.866	Cu: 2.37, 2.39, 2.41, 2.40, 2.45, 2.58, 2.61 Sb: 2.58, 2.61
Cu_3BiS_3	D_2^4; 19	7.790	10.416	6.762	Cu: 2.26, 2.27, 2.28, 2.31, 2.34, 2.57, 2.59 Bi: 2.57, 2.59
$CuSbS_2$	D_{2h}^{16}; 62	6.031	3.993	14.060	Cu: 2.32, 2.41; Sb: 2.41, 2.56, 3.06
$CuSbSe_2$	D_{2h}^{16}; 62	6.346	4.204	14.614	Cu: 2.44, 2.52; Sb: 2.56, 2.69, 3.16
$CuSbTe_2$	D_{2h}^{16}; 62	6.803	4.522	15.327	Cu: 2.59, 2.66; Sb: 2.89, 2.79, 3.33
$CuBiS_2$	D_{2h}^{16}; 62	6.199	4.087	14.115	Cu: 2.32, 2.43; Bi: 2.65, 3.09
$CuBiSe_2$	D_{2h}^{16}; 62	6.491	4.303	14.700	Cu: 2.43, 2.53; Bi: 2.67, 2.79, 3.20
$CuBiTe_2$	D_{2h}^{16}; 62	6.954	4.621	15.232	Cu: 2.59, 2.68; Bi: 2.88, 2.30, 3.37
$CuBi_2O_4$	D_{4h}^{8}; 130	8.635	8.635	5.845	Cu: 2.01; Bi: 2.14, 2.30, 2.80

Table 4.2 The direct $E_{g,dir}$ indirect, $E_{g,ind}$ and Γ-point $E_{g,\Gamma}$ band gap energies, obtained from the HSE06 calculations. The static ε_0 and high-frequency ε_∞ dielectric constants are presented in the three Cartesian directions *x*, *y* and *z*.

Compound	*Band gap energies [eV]*			*Static and high-frequency dielectric constants*					
	$E_{g,dir}$	$E_{g,ind}$	$E_{g,\Gamma}$	$\varepsilon_{0,xx}$	$\varepsilon_{0,yy}$	$\varepsilon_{0,zz}$	$\varepsilon_{\infty,xx}$	$\varepsilon_{\infty,yy}$	$\varepsilon_{\infty,zz}$
$CuGaSe_2$	1.47		1.47	9.6	9.6	10.2	7.0	7.0	7.0
$CuInSe_2$	0.85		0.85	11.8	11.8	13.0	7.4	7.4	7.4
$Cu_2ZnSnSe_4$	0.90		0.90	10.5	10.5	11.5	7.7	7.7	7.7
Cu_2ZnSnS_4	1.48		1.48	8.8	8.8	9.4	6.3	6.3	6.2
Cu_2ZnGeS_4	2.08		2.08	8.4	8.4	8.9	6.1	6.1	6.1
Cu_2ZnSiS_4	2.89		2.89	7.9	7.9	8.3	5.6	5.6	5.7
Cu_2CdSnS_4	1.22		1.22	9.4	9.4	20.7	6.1	6.1	6.6
Cu_2BeSnS_4	1.76		1.76	8.8	8.8	9.5	6.7	6.7	6.7
Cu_2MgSnS_4	1.48		1.48	8.6	8.6	8.3	6.0	6.0	6.6
Cu_2CaSnS_4	1.84		1.84	8.7	8.7	8.5	5.9	5.9	6.1
Cu_2SrSnS_4	1.81	1.80	1.81	11.0	11.0	10.1	5.7	5.7	5.6
Cu_2BaSnS_4	1.80	1.79	1.80	9. 6	9.6	9.1	5.7	5.7	5.6
$Cu_2SrSnSe_4$	1.59	1.55	1.59	12.3	12.4	11.8	6.8	6.3	7.4
$Cu_2BaSnSe_4$	1.65		1.65	11.4	11.3	11.0	6.6	6.3	6.8
Cu_2MnSnS_4	1.40		1.40	8.9	8.9	8.6	6.3	6.3	6.8
Cu_2FeSnS_4	1.71		1.71	8.8	8.8	8.4	6. 6	6. 6	6. 9
Cu_2NiSnS_4	1.26	1.17	1.26	9.6	10.0	8. 5	7.0	7.4	6.6
Cu_2O	2.06		2.06	6.8	6.8	6.8	5.6	5.6	5.6
Cu_2SnS_3	0.83		0.83	10.5	10.8	12.2	7.4	7.5	7.4
Cu_2GeS_3	1.42		1.42	9.1	9.3	10.7	7.0	7.1	7.2
Cu_2SiS_3	2.58		2.58	8.2	8.2	9.0	6.1	6.2	6.2
Cu_4SnS_4	0.52	0.42	0.52	12.8	33.5	12.1	9.5	10.9	8.6
Cu_4GeS_4	1.14	1.10	1.14	11.6	11.0	9.8	8.1	8.0	7.2
Cu_4SiS_4	1.95	1.82	1.95	11.4	40.0	8.9	7.0	6.7	6.4
Cu_4SiSe_4	0.87	0.65	0.87	12.9	16.4	11.6	8.8	9.1	8.6
Cu_3SbS_3	2.13	2.06	2.13	8.0	11.5	9.5	6.2	7.4	7.1
Cu_3SbSe_3	2.01	1.85	2.01	9.1	14.6	11.4	7.3	8.7	8.3
Cu_3BiS_3	1.88	1.75	1.88	11.6	13.4	10.8	7.3	7.9	7.5
$CuSbS_2$	1.37	1.25	1.40	11.6	41.6	14.1	8.5	10.8	8.9
$CuSbSe_2$	1.05	0.97	1.05	12.4	57.0	25.6	9.8	14.2	19.8
$CuSbTe_2$	0.92	0.63	0.92	13.4	103.1	19.0	11.9	20.7	14.5
$CuBiS_2$	1.61	1.35	1.61	12.4	36.0	13.9	8.8	10.1	8.8
$CuBiSe_2$	1.18	1.12	1.18	13.4	46.5	16.0	10.2	13.1	10.6
$CuBiTe_2$	1.04	0.84	1.04	14.2	65.4	19.2	12.3	18.2	13.9
$CuBi_2O_4$	1.24	1.18	1.24	18.8	18.8	22.0	5.4	5.4	4.9

Table 4.3 Same as Table 4.2 for selected complementary compounds.

Compound	*Band gap energies [eV]*			*Static and high-frequency dielectric constants*					
	$E_{g,dir}$	$E_{g,ind}$	$E_{g,\Gamma}$	$\varepsilon_{0,xx}$	$\varepsilon_{0,yy}$	$\varepsilon_{0,zz}$	$\varepsilon_{\infty,xx}$	$\varepsilon_{\infty,yy}$	$\varepsilon_{\infty,zz}$
$CuIn_{0.5}Ga_{0.5}Se_2$	1.21		1.21	11.4	11.4	12.6	7.1	7.1	7.1
GaAs	1.24		1.24	12.7	12.7	12.7	10.3	10.3	10.3
CdTe	1.45		1.45	10.4	10.4	10.4	6.6	6.6	6.6
Cu_3N	1.71	0.99	4.84	7.6	7.6	7.6	7.2	7.2	7.2
Cu_3P	1.58		5.37	6.2	6.2	6.2	6.1	6.1	6.1
$BaSi_2$	1.40	1.29	1.70	18.4	19.4	17.9	10.9	11.1	11.2
$BaGe_2$	1.15	1.00	1.50	20.1	21.6	20.3	12.3	13.0	12.8
$SrSi_2$	1.22	1.06	1.50	18.6	20.2	19.3	11.9	12.1	12.6
$SrGe_2$	1.06	0.78	1.28	21.4	24.1	22.8	13.7	14.6	14.7
GeSe	1.96	1.67	2.59	21.7	15.4	16.8	11.0	8.5	9.8
SnS	1.85	1.50	2.94	23.9	38.3	24.3	10.3	11.3	8.6
Sb_2Se_3	0.87	0.72	2.23	99.9	95.4	12.7	31.2	11.5	9.1
Bi_2S_3	1.01	0.79	2.30	89.8	83.7	21.9	19.8	11.2	13.5
Bi_2Se_3	1.06	0.68	1.63	92.1	95.2	26.8	27.5	13.6	18.6
$ZnSnN_2$	1.24		1.24	10.3	10.3	10.6	5.7	5.7	5.6
$ZnSnP_2$	1.71		1.71	11.2	11.2	11.3	8.8	8.8	8.7
Zn_3P_2	1.19		1.19	28.2	28.2	17.7	10.0	10.0	9.8

Table 4.4 Defect formation energy $\Delta H(D)$ for $\Delta\mu_\alpha = 0$ and the induced shift $\Delta E_g(D)$ of the gap energy for native defects in tetragonal or trigonal Cu_2XSnS_4 (X = Be, Mg, Ca, Mn, Fe, Ni, Cd and Zn); all values are in units of eV. The defect concentration is about 1.5%. Total magnetic moment M_t units in μ_B is given for magnetic compounds including the defects, where the local magnetic moment is ~4.4μ_B for Mn, ~3.5μ_B for Fe and ~1.5μ_B for Ni. The table is from Reference 85, though extended with X = Cd.

Compound	*Phase*	*Energy [eV]*	*Defect type D, where X is the group-II element*					
			V_{Cu}	V_X	X_{Cu}	Cu_X	$(V_{Cu}+X_{Cu})$	(Cu_X+X_{Cu})
Cu_2ZnSnS_4	S_4^2; 82	ΔH	1.42	3.54	0.45	1.64	−0.09	0.30
		ΔE_g	0.06	−0.03	−0.13	−0.12	0.08	−0.13
Cu_2CdSnS_4	D_{2d}^{11}; 121	ΔH	1.43	4.83	−0.75	2.89	−1.26	0.34
		ΔE_g	0.08	0.01	−0.10	−0.12	0.09	−0.09
Cu_2BeSnS_4	S_4^2; 82	ΔH	1.50	4.14	0.19	2.33	−0.28	0.58
		ΔE_g	0.00	−0.12	−0.22	−0.26	0.07	−0.30
Cu_2MgSnS_4	D_{2d}^{11} ; 121; AFM	ΔH	1.61	4.85	−0.52	2.83	−1.07	0.34
		ΔE_g	0.07	−0.07	−0.10	−0.22	0.10	−0.18
Cu_2CaSnS_4	D_{2d}^{11} ; 121	ΔH	1.14	5.92	−1.86	3.86	−2.68	0.13
		ΔE_g	−0.07	−0.14	−0.22	−0.34	0.02	−0.29
	C_3^2; 144	ΔH	1.27	5.69	−1.47	4.66	−2.05	1.40
		ΔE_g	0.04	−0.08	−0.74	−0.41	0.14	−0.29
Cu_2MnSnS_4	D_{2d}^{11} ; 121; AFM	ΔH	1.60	4.37	−0.21	2.35	−0.54	0.33
		ΔE_g	0.05	−0.35	−0.21	−0.37	0.06	−0.19
		M_t	0.1	3.0	4.6	4.0	5.0	0.0
Cu_2FeSnS_4	D_{2d}^{11} ; 121; AFM	ΔH	1.64	5.94	−1.67	3.81	−2.01	0.35
		ΔE_g	−0.02	−0.83	−1.08	−0.26	0.01	−0.17
		M_t	0.3	2.0	2.8	2.8	3.7	0
Cu_2NiSnS_4	S_4^2; 82; AFM	ΔH	1.57	3.09	−0.22	1.08	0.60	0.36
		ΔE_g	−0.07	−0.18	0.00	−0.22	−0.15	−0.53
		M_t	0.1	2.0	1.0	2.8	2.0	0.0

Figure Captions

Figure 4.1 Crystalline structures of various Cu-based chalcogenides. In the figures, Cu atoms are in dark blue colour, Sn atoms are in grey, S atoms are in yellow and O atoms are in red colour.

Figure 4.2 (a) The calculated electronic band structure of $CuIn_{0.5}Ga_{0.5}Se_2$ where the critical points are identified along the main symmetry directions. (b) Band-to-band analysis of the contribution to the total $\varepsilon_2(E)$ spectrum (thin black trace) and the individual critical points. The most important VB-to-CB transitions ($v_j \rightarrow v_{j'}$) are marked by thick coloured curves. Spin-orbit interaction is included and the band-to-band transitions involve a summation of the spin-up and spin-down like contributions. Note: The vertical axis ε_2 is in the logarithmic scale. The results were obtained with the FPLAPW approach as implemented in the WIEN2k code, using the PBE+U potential with U_d(Cu) = 6 eV. The figure is from Reference 69.

Figure 4.3 Calculated imaginary part $\varepsilon_2(E)$ of the dielectric function for kesterite Cu_2ZnSnS_4 using PBE, PBE+U (with U_d(Cu) = 4.0 eV) and HSE06 with the $\mathbf{k} \cdot \tilde{\mathbf{p}}$ method as described in Reference 72. The band gap energies have been shifter to agree with that of HSE06. A **k**-mesh with grid size 24×24×24 gives good absorption onset feature also near the band gap energy.

Figure 4.4 The imaginary part $\varepsilon_2(E)$ of the dielectric function for monoclinic Cu_2SiS_3 with the HSE06 and gap-corrected PBE+U computational approaches. All spectra has the onset at $E_g = E_A = 2.60$ eV, determined from the HSE06 calculation. First, we demonstrates that the PBE [i. e., with no onsite Coulomb potential, thus U_d(Cu) = 0 eV; see (a)] generates qualitatively the same near-gap spectra as PBE+U [with U_d(Cu) = 6 eV; see (b)] near the band-edge energy. Second, with a sparse 5×5×5 **k**-mesh (implying $N_{\mathbf{k}} = 39$ **k**-points in the IBZ) both HSE06 (light blue lines) and PBE+U (purple lines) show qualitatively the same spectra with no indication of a double onset near E_g. Third, with a denser 20×20×20 **k**-mesh (2121 **k**-points; red lines) and 30×30×30 **k**-mesh (6992 **k**-points; black lines) the double onset is clear and one actually observes the contributions from the three transitions $E_A = 2.60$ eV, $E_B = 2.76$ eV and $E_C = 2.83$ eV; compare with Fig. 4.X in the main article. The figure is from Supplementary data in Reference 28.

Figure 4.5 (a) The Shockley-Queisser (SQ) limit as function of the band gap energy E_g for an infinite thick solar cell absorber, thus $d \rightarrow \infty$. The maximum efficiency η_{max} is obtained for E_g = 1.2–1.4 eV. (b) The thickness dependent maximum efficiency η_{max} for $CuIn_{1-x}Ga_xSe_2$ (≡ CIGS) for x = 0.0, 0.5 and 1.0 with the

gap energies E_g = 0.85, 1.21 and 1.47 eV, respectively. Notice logarithm scale for the thickness (i. e., the *x*-axis). One can notice that the efficiencies drop substantially around 500–800 nm.

Figure 4.6 (a) Upper panel shows the mixing energy (eV/cell where cell has 16 atoms) of $Cu_2ZnSn_{1-x}Ge_xS_4$, $Cu_2ZnSn_{1-x}Si_xS_4$, $Cu_2ZnSn_{1-x}Ge_xSe_4$ and $Cu_2ZnSn_{1-x}Si_xSe_4$ as functions of alloy compositions x = 0, 0.5 and 1 computed by using the HSE06 hybrid functional. Lower panel present the band gap energies E_g, where HSE06 underestimates the gap energies by about 0.1–0.4 eV for all compounds compared to experimental data. (b) Corresponding absorption coefficients $\alpha(E)$.

Figure 4.7 The atom and angular-momentum resolved DOS (i. e., the PDOS) obtained with HSE06 and presented with a 0.1 eV post-calculated Lorentzian smearing and where the energy scales refer to the VBM. The PDOS has been weighted by $1/(2l + 1)$ for better visibility of *s*- and *p*-like states. (a) Cu_2ZnSnS_4, (b) Cu_2BaSnS_4, (or $Cu_2BaSnSe_4$ (c) Cu_2SnS_3 and (d) $CuSbS_2$.

Figure 4.8 (a) Electronic band structure of monoclinic Cu_2SnS_3 (CTS) along two main symmetry directions, i. e., (010) and (001), computed with the HSE06 potential. At the Γ-point VBM, there are three close-lying VBs (see inset figure) that contribute to the observed double absorption onset near the band gap energy. The marks indicate the main character of the energy states. The upper panel shows the optical interband matrix elements for electric dipole induced transitions. Each line colour refers to a specific VB for the transition $v_j \rightarrow c_1$ and each marker type refers to as specific polarization of the matrix element $M^{\alpha\alpha}$. Blue, red and black lines represent transitions from the uppermost (v_1), the second upper most (v_2) and the third uppermost (v_1) VBs, respectively, to the lowest CB (c_1). Square, cross and diamond markers represent *x*-, *y*- and *z*-polarized transitions respectively.

Figure 4.9 Polarization dependency of the dielectric function of CTS from the PBE+U approach with corrected gap energy. The calculated dielectric response $\varepsilon_2(E)$ is very anisotropic in the near-band-gap spectral region. The primitive cell of the crystal is defined by the lattice vectors $\mathbf{a}_1$, $\mathbf{a}_2$ and $\mathbf{a}_3$ and the orientation of the polarization is described in the Cartesian coordinate space.

Figure 4.10 The real part ($\varepsilon_1(E)$; left panels) and the left part ($\varepsilon_2(E)$; right panels) of the complex dielectric functions $\varepsilon(E) = \varepsilon_1(E) + i\varepsilon_2(E)$, obtained with a **k**-mesh corrected HSE06 approach and with a 0.1 eV post-

prepared Gaussian broadening. The ionic contribution for $E \approx 0$ eV from electron optical-phonon interaction is not presented.

Figure 4.11 The absorption coefficient $\alpha(E)$, obtained directly from $\varepsilon(E)$ in Figure 4.10 and the energy scale refers to the fundamental gap energy (i. e., $\hbar\omega - E_g$) to better compare the spectra of compounds with different gap energies.

Figure 4.12 The maximum solar energy efficiency η_{max} as function of film thickness d. In subfigure (f) the dotted lines represent the efficiency if the Auger effect is excluded.

THE FOLLOWING IMAGES SHOULD BE SUPPLIED AS SEPARATE FILES in one of the following formats: TIFF/PDF /EPS/ DOC/XLS/PPT/JPEG/CDX.

Figure 4.1

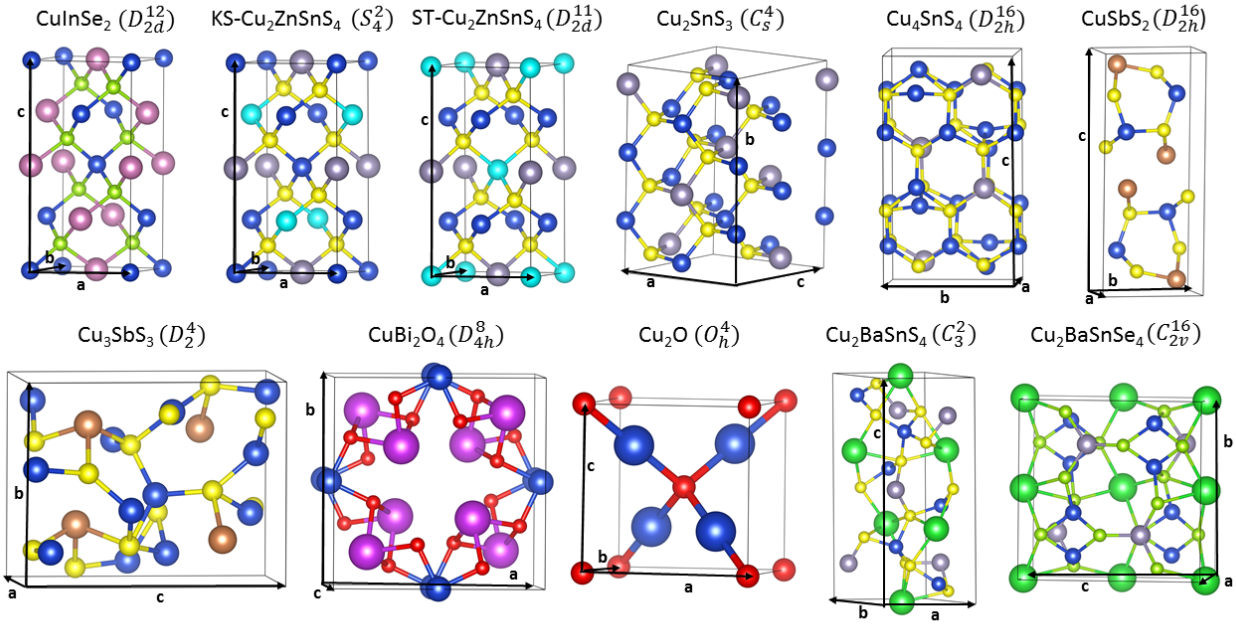

Figure 4.2

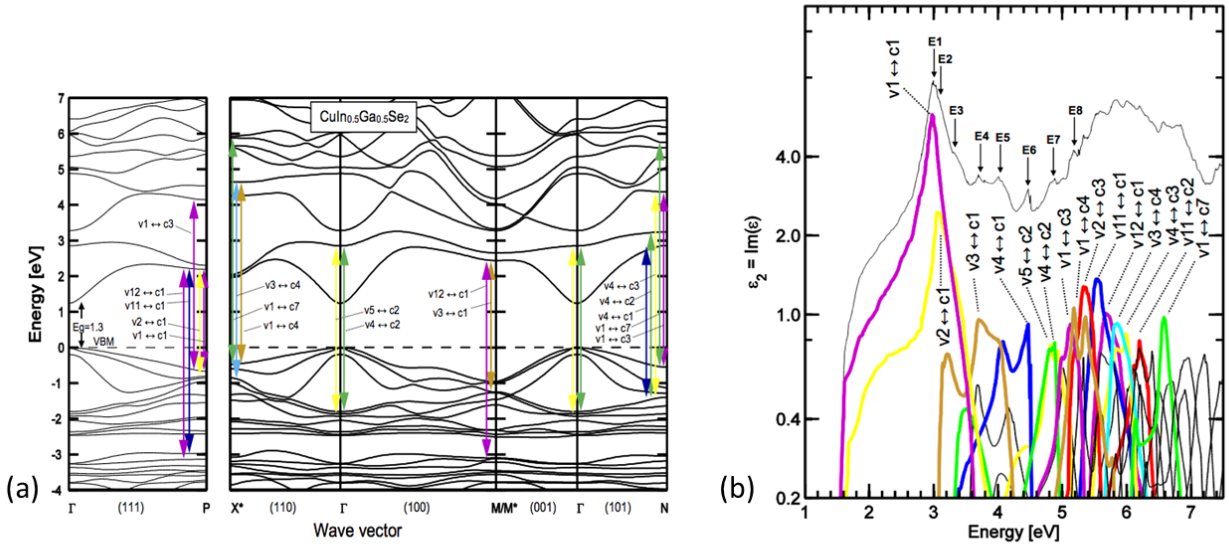
(a)
Energy [eV]
CuIn0.5Ga0.5Se2
Γ (111) P
X* (110) Γ (100) M/M* (001) Γ (101) N
Wave vector
(b)
ε2 = Im(ε)
Energy [eV]
E1
E2
E3
E4
E5
E6
E7
E8
v1 ↔ c1
v2 ↔ c1
v3 ↔ c1
v4 ↔ c1
v5 ↔ c2
v4 ↔ c2
v1 ↔ c3
v1 ↔ c4
v2 ↔ c3
v11 ↔ c1
v12 ↔ c1
v3 ↔ c4
v4 ↔ c3
v11 ↔ c2
v1 ↔ c7

Figure 4.3

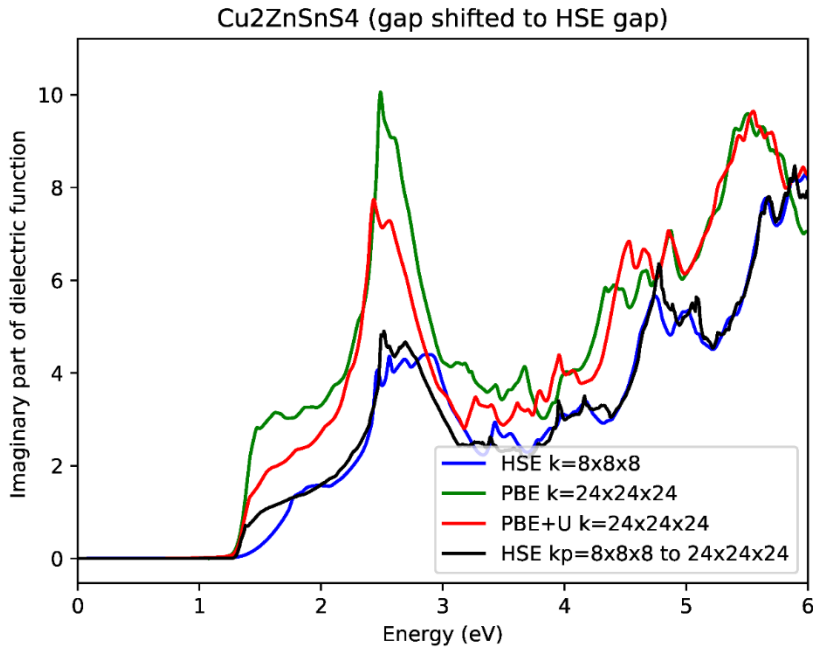
Cu2ZnSnS4 (gap shifted to HSE gap)
Imaginary part of dielectric function
Energy (eV)
HSE k=8x8x8
PBE k=24x24x24
PBE+U k=24x24x24
HSE kp=8x8x8 to 24x24x24

Figure 4.4

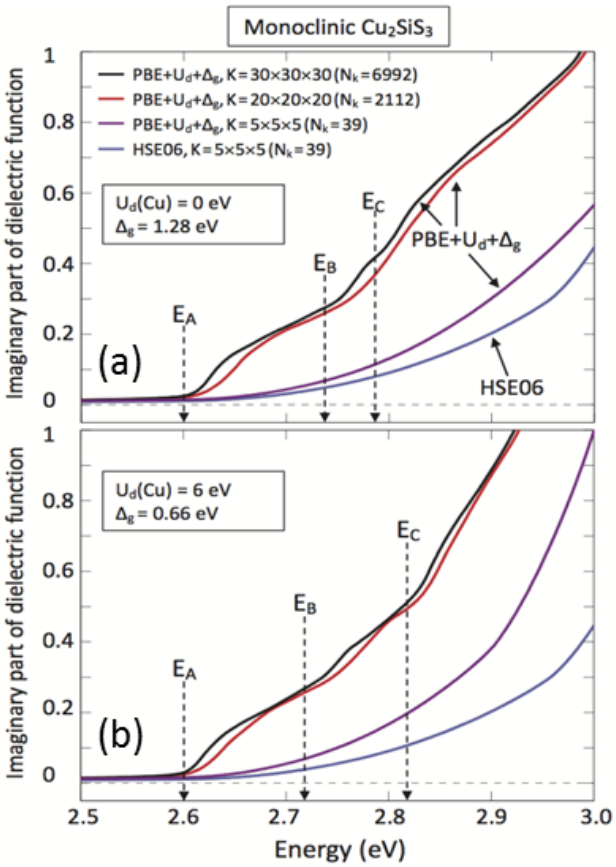
Monoclinic Cu_2SiS_3
PBE+U_d+Δ_g, K=30×30×30 (N_k=6992)
PBE+U_d+Δ_g, K=20×20×20 (N_k=2112)
PBE+U_d+Δ_g, K=5×5×5 (N_k=39)
HSE06, K=5×5×5 (N_k=39)
U_d(Cu) = 0 eV
Δ_g = 1.28 eV
E_A
E_B
E_C
PBE+U_d+Δ_g
HSE06
(a)
U_d(Cu) = 6 eV
Δ_g = 0.66 eV
(b)
Imaginary part of dielectric function
Energy (eV)
0
0.2
0.4
0.6
0.8
1
2.5
2.6
2.7
2.8
2.9
3.0

Figure 4.5

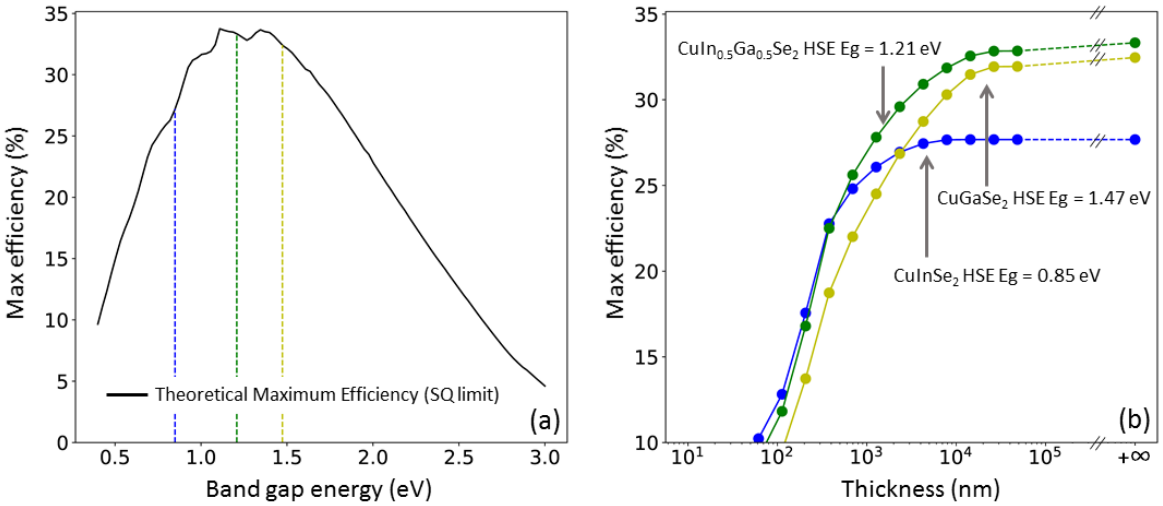
Max efficiency (%)
Band gap energy (eV)
Theoretical Maximum Efficiency (SQ limit)
(a)
CuIn0.5Ga0.5Se2 HSE Eg = 1.21 eV
CuGaSe2 HSE Eg = 1.47 eV
CuInSe2 HSE Eg = 0.85 eV
Thickness (nm)
(b)

Figure 4.6

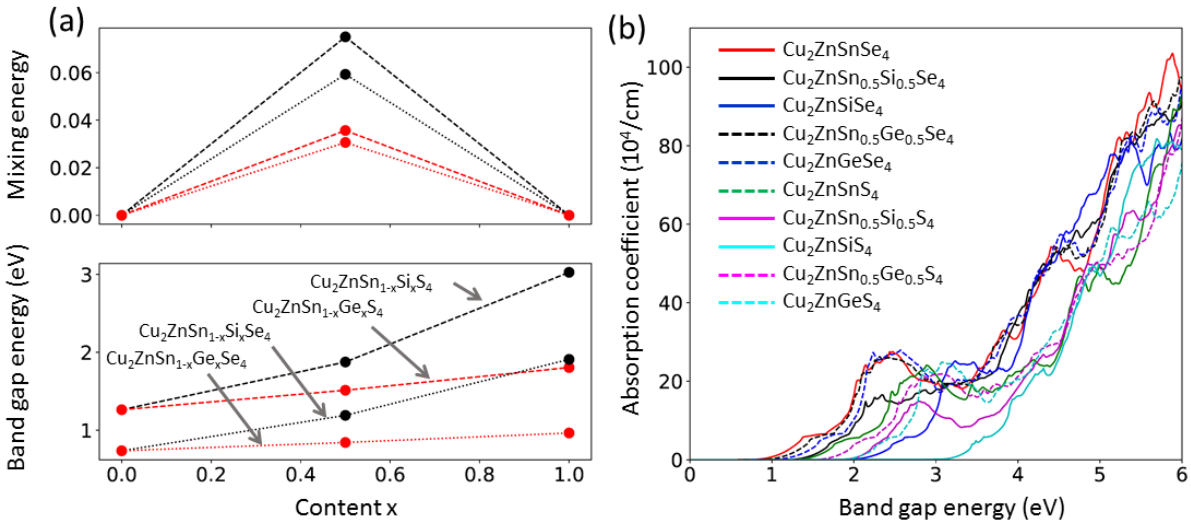
(a)
Mixing energy
0.06
0.04
0.02
0.00
Band gap energy (eV)
3
2
1
Cu2ZnSn1-xSixS4
Cu2ZnSn1-xGexS4
Cu2ZnSn1-xSixSe4
Cu2ZnSn1-xGexSe4
0.0
0.2
0.4
0.6
0.8
1.0
Content x
(b)
Absorption coefficient (10^4/cm)
100
80
60
40
20
0
Cu2ZnSnSe4
Cu2ZnSn0.5Si0.5Se4
Cu2ZnSiSe4
Cu2ZnSn0.5Ge0.5Se4
Cu2ZnGeSe4
Cu2ZnSnS4
Cu2ZnSn0.5Si0.5S4
Cu2ZnSiS4
Cu2ZnSn0.5Ge0.5S4
Cu2ZnGeS4
0
1
2
3
4
5
6
Band gap energy (eV)

Figure 4.7

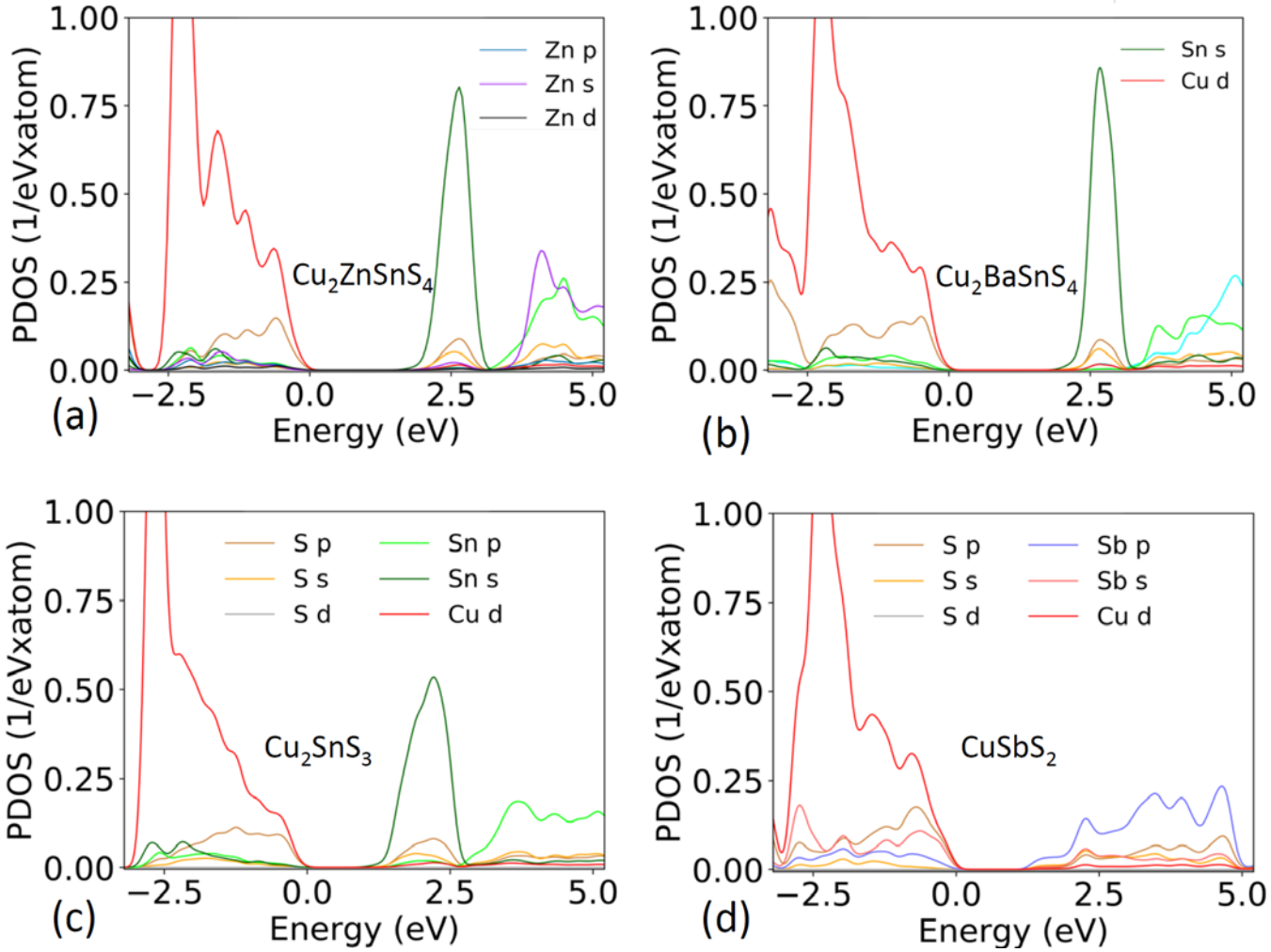
PDOS (1/eVxatom)
Energy (eV)
Zn p
Zn s
Zn d
Cu_2ZnSnS_4
(a)
Sn s
Cu d
Cu_2BaSnS_4
(b)
S p
S s
S d
Sn p
Sn s
Cu d
Cu_2SnS_3
(c)
Sb p
Sb s
$CuSbS_2$
(d)

Figure 4.8

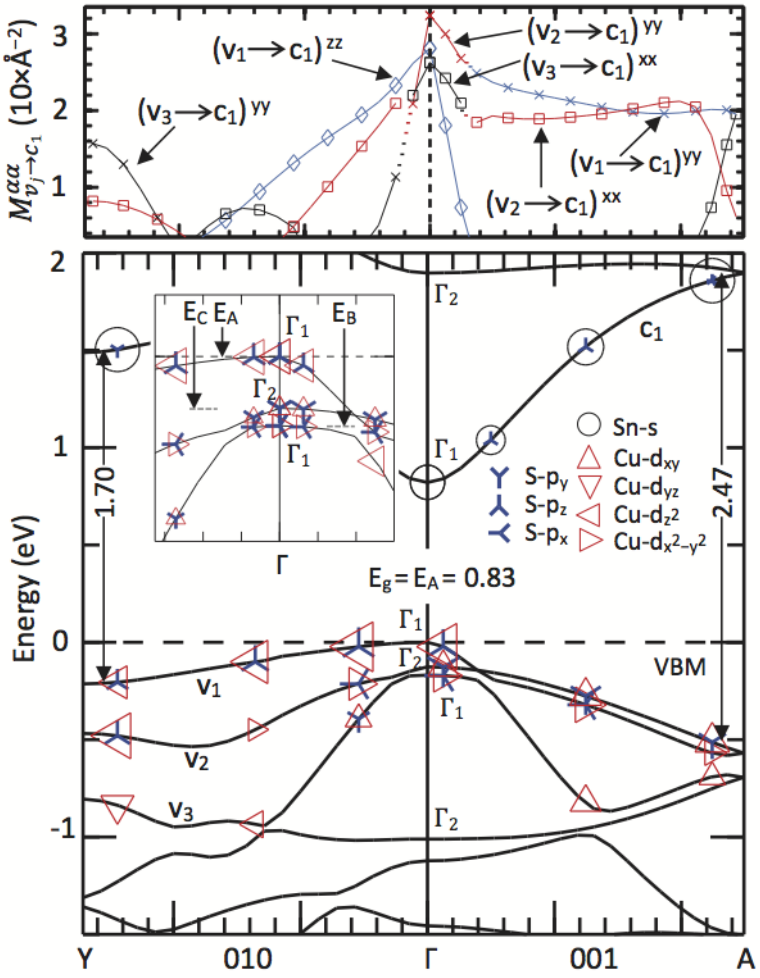
$M^{\alpha\alpha}_{v_j \to c_1}$ (10×Å^{-2})
$(v_1 \to c_1)^{zz}$
$(v_2 \to c_1)^{yy}$
$(v_3 \to c_1)^{xx}$
$(v_3 \to c_1)^{yy}$
$(v_1 \to c_1)^{yy}$
$(v_2 \to c_1)^{xx}$
Energy (eV)
E_C E_A
E_B
Γ_1
Γ_2
Γ
1.70
2.47
c_1
v_1
v_2
v_3
VBM
$E_g = E_A = 0.83$
Sn-s
Cu-d_{xy}
Cu-d_{yz}
Cu-d_{z^2}
Cu-$d_{x^2-y^2}$
S-p_y
S-p_z
S-p_x
Y
010
Γ
001
A

Figure 4.9

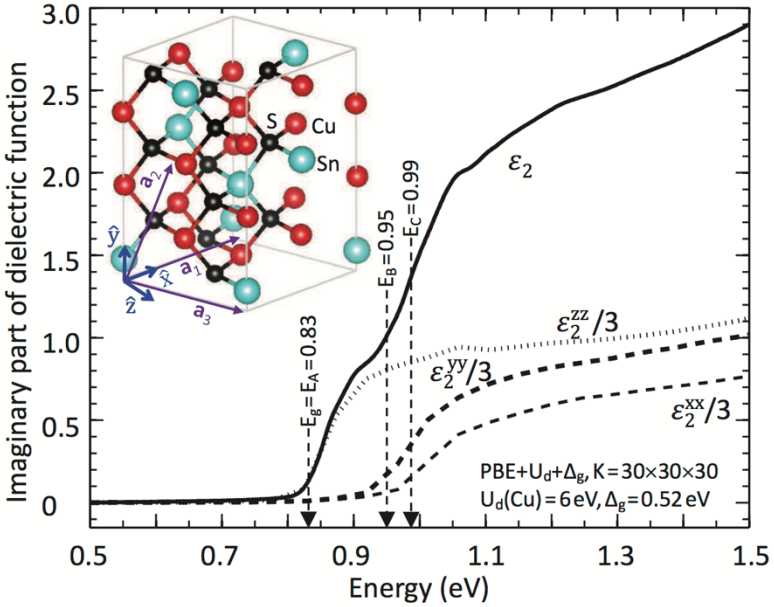
Imaginary part of dielectric function
Energy (eV)
3.0
2.5
2.0
1.5
1.0
0.5
0
0.5
0.7
0.9
1.1
1.3
1.5
S
Cu
Sn
a_1
a_2
a_3
$\hat{x}$
$\hat{y}$
$\hat{z}$
$E_g = E_A = 0.83$
$E_B = 0.95$
$E_C = 0.99$
ε_2
$\varepsilon_2^{zz}/3$
$\varepsilon_2^{yy}/3$
$\varepsilon_2^{xx}/3$
PBE+U_d+Δ_g, K=30×30×30
U_d(Cu)=6 eV, Δ_g=0.52 eV

Figure 4.10

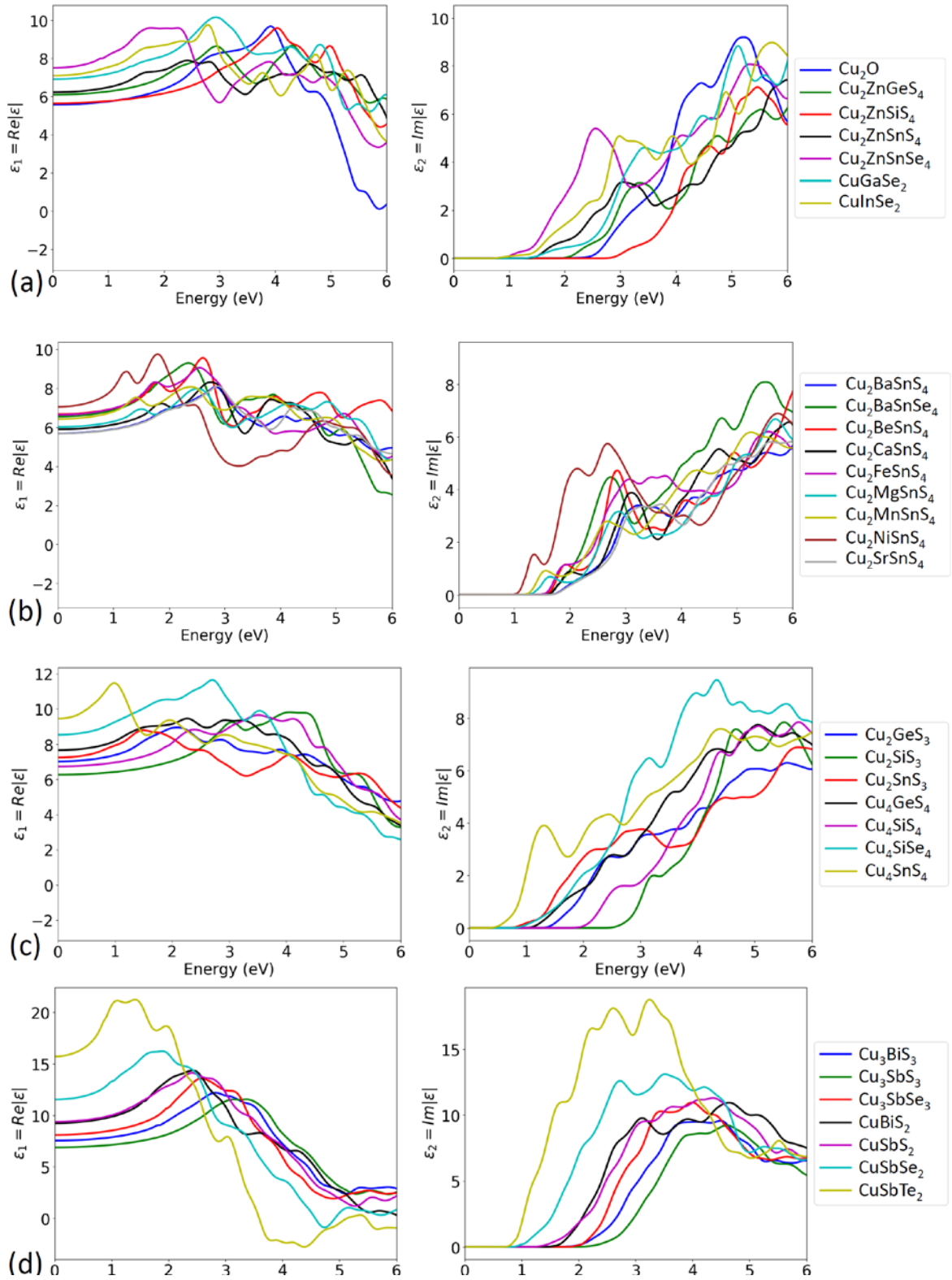
(a)
$\varepsilon_1 = Re|\varepsilon|$
$\varepsilon_2 = Im|\varepsilon|$
Energy (eV)
Cu_2O
Cu_2ZnGeS_4
Cu_2ZnSiS_4
Cu_2ZnSnS_4
$Cu_2ZnSnSe_4$
$CuGaSe_2$
$CuInSe_2$
(b)
$\varepsilon_1 = Re|\varepsilon|$
$\varepsilon_2 = Im|\varepsilon|$
Energy (eV)
Cu_2BaSnS_4
$Cu_2BaSnSe_4$
Cu_2BeSnS_4
Cu_2CaSnS_4
Cu_2FeSnS_4
Cu_2MgSnS_4
Cu_2MnSnS_4
Cu_2NiSnS_4
Cu_2SrSnS_4
(c)
$\varepsilon_1 = Re|\varepsilon|$
$\varepsilon_2 = Im|\varepsilon|$
Energy (eV)
Cu_2GeS_3
Cu_2SiS_3
Cu_2SnS_3
Cu_4GeS_4
Cu_4SiS_4
Cu_4SiSe_4
Cu_4SnS_4
(d)
$\varepsilon_1 = Re|\varepsilon|$
$\varepsilon_2 = Im|\varepsilon|$
Cu_3BiS_3
Cu_3SbS_3
Cu_3SbSe_3
$CuBiS_2$
$CuSbS_2$
$CuSbSe_2$
$CuSbTe_2$

Figure 4.11

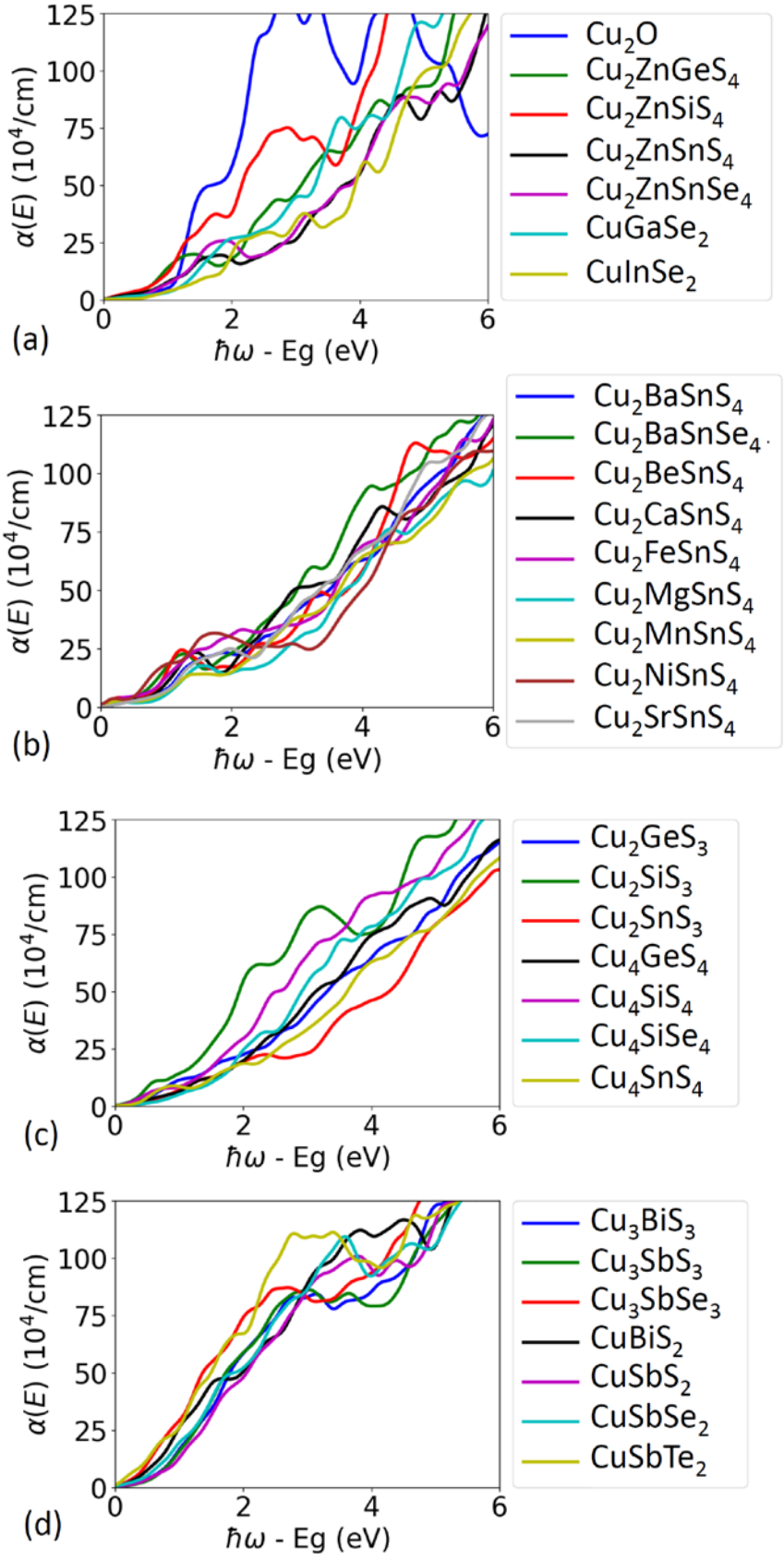
α(E) (10⁴/cm)
ħω - Eg (eV)
(a)
Cu2O
Cu2ZnGeS4
Cu2ZnSiS4
Cu2ZnSnS4
Cu2ZnSnSe4
CuGaSe2
CuInSe2
(b)
Cu2BaSnS4
Cu2BaSnSe4
Cu2BeSnS4
Cu2CaSnS4
Cu2FeSnS4
Cu2MgSnS4
Cu2MnSnS4
Cu2NiSnS4
Cu2SrSnS4
(c)
Cu2GeS3
Cu2SiS3
Cu2SnS3
Cu4GeS4
Cu4SiS4
Cu4SiSe4
Cu4SnS4
(d)
Cu3BiS3
Cu3SbS3
Cu3SbSe3
CuBiS2
CuSbS2
CuSbSe2
CuSbTe2

Figure 4.12

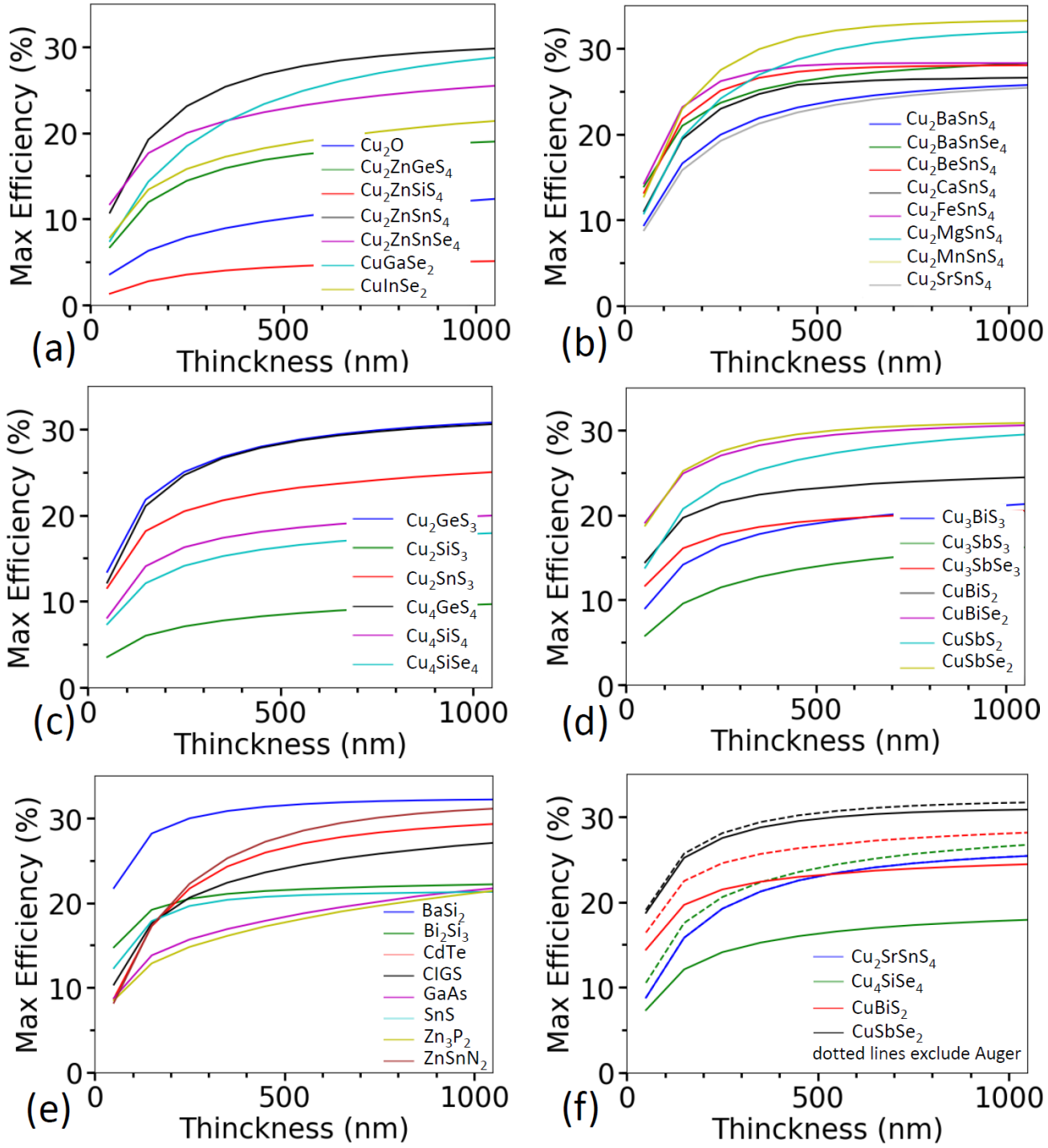
Max Efficiency (%)
Thinckness (nm)
(a)
Cu2O
Cu2ZnGeS4
Cu2ZnSiS4
Cu2ZnSnS4
Cu2ZnSnSe4
CuGaSe2
CuInSe2
(b)
Cu2BaSnS4
Cu2BaSnSe4
Cu2BeSnS4
Cu2CaSnS4
Cu2FeSnS4
Cu2MgSnS4
Cu2MnSnS4
Cu2SrSnS4
(c)
Cu2GeS3
Cu2SiS3
Cu2SnS3
Cu4GeS4
Cu4SiS4
Cu4SiSe4
(d)
Cu3BiS3
Cu3SbS3
Cu3SbSe3
CuBiS2
CuBiSe2
CuSbS2
CuSbSe2
(e)
BaSi2
Bi2Si3
CdTe
CIGS
GaAs
SnS
Zn3P2
ZnSnN2
(f)
Cu2SrSnS4
Cu4SiSe4
CuBiS2
CuSbSe2
dotted lines exclude Auger